

CLUSTER MASS PROFILES FROM A BAYESIAN ANALYSIS OF WEAK LENSING DISTORTION AND
MAGNIFICATION MEASUREMENTS: APPLICATIONS TO SUBARU DATA ¹KEIICHI UMETSU², TOM BROADHURST^{3,4}, ADI ZITRIN⁵, ELINOR MEDEZINSKI⁶, LI-YEN HSU⁷*Draft version June 26, 2012*

ABSTRACT

We directly construct model-independent mass profiles of galaxy clusters from combined weak-lensing distortion and magnification measurements within a Bayesian statistical framework, which allows for a full parameter-space extraction of the underlying signal. This method applies to the full range of radius outside the Einstein radius, and recovers the absolute mass normalization. We apply our method to deep Subaru imaging of five high-mass ($> 10^{15} M_{\odot}$) clusters, A1689, A1703, A370, Cl0024+17, and RXJ1347-11, to obtain accurate profiles to beyond the virial radius (r_{vir}). For each cluster the lens distortion and magnification data are shown to be consistent with each other, and the total signal-to-noise ratio of the combined measurements ranges from 13 to 24 per cluster. We form a model-independent mass profile from stacking the clusters, which is detected at 37σ out to $R \approx 1.7r_{\text{vir}}$. The projected logarithmic slope $\gamma_{2D}(R) \equiv d \ln \Sigma / d \ln R$ steepens from $\gamma_{2D} = -1.01 \pm 0.09$ at $R \approx 0.1r_{\text{vir}}$ to $\gamma_{2D} = -1.92 \pm 0.51$ at $R \approx 0.9r_{\text{vir}}$. We also derive for each cluster inner strong-lensing based mass profiles from deep Advanced Camera for Surveys observations with the *Hubble Space Telescope*, which we show overlap well with the outer Subaru-based profiles and together are well described by a generalized form of the Navarro-Frenk-White profile, except for the ongoing merger RXJ1347-11, with modest variations in the central cusp slope ($-d \ln \rho / d \ln r \lesssim 0.9$). The improvement here from adding the magnification measurements is significant, $\sim 30\%$ in terms of cluster mass profile measurements, compared with the lensing distortion signal.

Keywords: cosmology: observations — dark matter — galaxies: clusters: individual (A1689, A1703, A370, Cl0024+1654, RXJ1347-1145) — gravitational lensing: weak — gravitational lensing: strong

1. INTRODUCTION

Galaxy clusters provide an independent means of examining any viable model of cosmic structure formation through the growth of structure and by the form of their equilibrium mass profiles, complementing cosmic microwave background and galaxy clustering observations. A consistent framework of structure formation requires that most of the matter in the Universe is in the hitherto unknown form of dark matter, of an unknown nature, and that most of the energy filling the Universe today is in the form of a mysterious “dark energy”, characterized by a negative pressure. This model actually requires that the expansion rate of the Universe has recently changed sign and is currently accelerating.

Clusters play a direct role in testing cosmological models, providing several independent checks of any viable cosmology, including the current consensus Λ cold dark matter (Λ CDM) model. A spectacular example has

been recently provided from detailed lensing and X-ray observations of the “Bullet Cluster” (aka, IE0657-56; Markevitch et al. 2004; Clowe et al. 2006), which is a consequence of a high-speed collision between two cluster components with a mass ratio of the order of 6 : 1 (Mastropietro & Burkert 2008), displaying a prominent bow shock preceding a cool bullet lying between the two clusters, implying these clusters passed through each other recently (Markevitch et al. 2002, 2004). Here the Bullet system reveals lensing mass contours that follow the bimodal distribution of cluster members, demonstrating that the bulk of the dark matter is relatively collisionless as galaxies (Clowe et al. 2006), as also shown by a comprehensive analysis of galaxy and dark-matter dynamics for A1689 (Lemze et al. 2011). Other cases of merging systems show that in general displacement of the hot gas relative to the dark matter is related to interaction (Jee et al. 2005; Okabe & Umetsu 2008). For dynamically-relaxed clusters, the form of the equilibrium mass profile reflects closely the distribution of dark matter (see Mead et al. 2010) which, unlike galaxies, does not suffer from halo compression by adiabatic contraction of cooled gas. The majority of baryons in clusters are in the form of hot, diffuse X-ray emitting gas, and represents only a minor fraction of the total lensing mass near the centers of clusters (Lemze et al. 2008; Umetsu et al. 2009).

The predicted Navarro-Frenk-White profile (hereafter, NFW; Navarro et al. 1996, 1997) derived from simulations based on collisionless, cold (non-relativistic) dark matter has a continuously-declining logarithmic gradi-

¹ Based in part on data collected at the Subaru Telescope, which is operated by the National Astronomical Society of Japan.

² Institute of Astronomy and Astrophysics, Academia Sinica, P. O. Box 23-141, Taipei 10617, Taiwan.

³ Theoretical physics, University of the Basque Country, Bilbao 48080, Spain.

⁴ Ikerbasque, Basque Foundation for Science, Alameda Urquijo, 36-5 Plaza Bizkaia 48011, Bilbao, Spain.

⁵ School of Physics and Astronomy, Tel Aviv University, Tel Aviv 69978, Israel.

⁶ Johns Hopkins University, 3400 North Charles Street, Baltimore, MD 21218, USA.

⁷ Leung center for Cosmology and Particle Astrophysics, National Taiwan University, Taipei 10617, Taiwan.

ent $\gamma_{3D}(r) = d \ln \rho / d \ln r$ towards the center of mass, much shallower than the isothermal case ($\gamma_{3D} = -2$) within the characteristic scale radius, r_s ($\lesssim 300 \text{ kpc } h^{-1}$ for cluster-sized halos). A useful index of the degree of concentration, c_{vir} , compares the virial radius, r_{vir} , to r_s of the NFW profile, $c_{\text{vir}} \equiv r_{\text{vir}}/r_s$. This has been confirmed thoroughly with higher resolution simulations (Ghigna et al. 1998; Fukushige & Makino 1997; Okamoto & Habe 1999; Power et al. 2003; Navarro et al. 2004; Neto et al. 2007), with some intrinsic variation related to the individual assembly history of a cluster (Jing & Suto 2000; Tasitsiomi et al. 2004). Gravitational lensing observations are underway to provide reliable and representative cluster mass profiles to test this since the first careful measurements showed that the NFW profile provides a good fit to the entire mass profile when weak and strong lensing are combined (Gavazzi et al. 2003; Broadhurst et al. 2005a, 2008; Umetsu et al. 2010). Other well studied clusters with similarly high quality data are also in good agreement providing strong support for the CDM scenario (e.g., Okabe et al. 2010).

Interestingly these studies reveal that although the dark matter is consistent with being cold, the predicted profile concentration of the standard Λ CDM model falls short of some lensing results (e.g., Broadhurst et al. 2005a, 2008; Oguri et al. 2009). This observed tendency for higher proportion of mass to lie at smaller radius in projection is also indicated by the generally large Einstein radii determined from strong lensing of well studied clusters (Broadhurst & Barkana 2008; Zitrin et al. 2011) finding a substantial discrepancy with the predictions despite careful accounting for potential selection biases inherent to lensing (Hennawi et al. 2007; Meneghetti et al. 2010a). These observations could suggest either substantial mass projected along the line of sight, perhaps in part due to halo triaxiality (Oguri et al. 2005), or a large overconcentration of mass; the latter could imply modification within the context of the CDM family of models.

The abundance of massive clusters is very sensitive to the amplitude of the initial mass power spectrum (Sheth et al. 2001) representing the most massive objects to have collapsed under their own gravity, and confirmed by N -body simulations of Hubble volumes (Evrard et al. 2002). Such calculations predict for example that the single most massive cluster to be found in the universe is expected to be with $M_{\text{vir}} = 4 \times 10^{15} M_{\odot}$ out to $z = 0.4$ (see Figure 5 of Broadhurst & Barkana 2008), similar to the most massive known clusters detected locally (Broadhurst et al. 2008).⁸ At higher redshifts this comparison becomes more sensitive to the cosmological model, with an order of magnitude decline in the abundance of $10^{15} M_{\odot}$ clusters at $z > 0.8$ compared to the present (Evrard et al. 2002). Hence, the existence of such massive clusters like XMMUJ2235-25 at $z = 1.45$ (Jee et al. 2009), from lensing work, begins to motivate alternative ideas such as departures from Gaussian initial density fluctuation spectrum, or higher levels of dark energy in the past (Sadeh & Rephaeli 2008), although some non-Gaussian models can be ruled out by using the cosmic X-ray background measurements (Lemze et al.

2009b).

The main attraction of gravitational lensing in the cluster regime (e.g., Hattori et al. 1999; Umetsu et al. 1999; Bartelmann & Schneider 2001; Umetsu 2010) is the model-free determination of mass profiles allowed over a wide range of radius when the complementary effects of strong and weak lensing are combined (Broadhurst et al. 2005a; Umetsu & Broadhurst 2008; Merten et al. 2009; Umetsu et al. 2010; Meneghetti et al. 2010b; Zitrin et al. 2010). In practice, the quality of data required challenges with few facilities, which are able to generate data of sufficient precision to provide a significant detection of the weak lensing signal on an individual cluster basis.

In this paper we aim to pursue in greater depth the utility of massive clusters for defining highest-precision mass profiles by combining all lensing information available in the cluster regime. In particular, we shall make a full use of the magnification information, afforded by measuring spatial variations in the surface number density of faint background galaxies (Broadhurst et al. 1995; Taylor et al. 1998; Zhang & Pen 2005; Umetsu & Broadhurst 2008; Rozo & Schmidt 2010; Van Waerbeke et al. 2010), which we show here is readily detectable in the high-quality images we have obtained for this purpose. In our earlier work, particularly on A1689 and Cl0024+17, the magnification information determined from the background counts was used only as a consistency check of distortion measurements (Broadhurst et al. 2008; Umetsu et al. 2010). Recently, we have shown in Umetsu & Broadhurst (2008) how to overcome the intrinsic clustering of background galaxies, which otherwise perturbs locally the magnification signal, and how to combine the two independent weak-lensing data sets to improve the quality of two-dimensional mass reconstruction using regularized maximum-likelihood techniques. Here we further explore new statistical methods designed to obtain an optimal combination of the complementary lens distortion and magnification effects. Our aim here is to develop and apply techniques to a sample of five well-studied, high-mass clusters with $M \gtrsim 10^{15} M_{\odot}$, A1689, A1703, A370, Cl0024+17, and RXJ1347-11, for examining the underlying mass profiles extracted from the combined weak-lensing data sets. We then add to this detailed strong-lensing information for the inner $\lesssim 200 \text{ kpc}$ region of these clusters, for which we have identified many new sets of multiple images from Advanced Camera for Surveys (ACS) observations (Broadhurst et al. 2005b; Zitrin et al. 2009, 2010) with the *Hubble Space Telescope* (*HST*), to derive improved inner mass profiles for a full determination of the entire mass profiles of the five well-studied clusters.

The paper is organized as follows. We briefly summarize in § 2 the basis of cluster weak gravitational lensing. In § 3 we present our comprehensive lensing method in a Bayesian framework for a direct reconstruction of the projected cluster mass profile from combined weak-lensing shape distortion and magnification bias measurements. In § 4 we apply our method to Subaru weak-lensing observations of five massive clusters to derive projected mass profiles to beyond the cluster virial radius; we also combine our new weak-lensing mass profiles with inner strong-lensing based information from *HST*/ACS observations to make a full determination of the entire

⁸ A370 at $z = 0.375$ is currently the most massive known cluster measured reliably by lensing, $M_{\text{vir}} = (2.9 \pm 0.3) \times 10^{15} M_{\odot}$.

cluster mass profiles. Finally, summary and discussions are given in § 5.

Throughout this paper, we use the AB magnitude system, and adopt a concordance Λ CDM cosmology with $\Omega_m = 0.3$, $\Omega_\Lambda = 0.7$, and $h \equiv H_0/(100 \text{ km s}^{-1} \text{ Mpc}^{-1}) = 0.7$. Errors represent a confidence level of 68.3% (1σ) unless otherwise stated.

2. BASIS OF CLUSTER WEAK LENSING

The deformation of the image for a background source can be described by the Jacobian matrix $\mathcal{A}_{\alpha\beta}$ ($\alpha, \beta = 1, 2$) of the lens mapping.⁹ The real, symmetric Jacobian $\mathcal{A}_{\alpha\beta}$ can be decomposed as $\mathcal{A}_{\alpha\beta} = (1 - \kappa)\delta_{\alpha\beta} - \Gamma_{\alpha\beta}$, where $\delta_{\alpha\beta}$ is Kronecker's delta, κ is the lensing convergence, and $\Gamma_{\alpha\beta}$ is the trace-free, symmetric shear matrix,

$$\Gamma_{\alpha\beta} = \begin{pmatrix} +\gamma_1 & \gamma_2 \\ \gamma_2 & -\gamma_1 \end{pmatrix}, \quad (1)$$

with γ_α being the components of spin-2 complex gravitational shear $\gamma := \gamma_1 + i\gamma_2$. In the strict weak lensing limit where $\kappa, |\gamma| \ll 1$, $\Gamma_{\alpha\beta}$ induces a quadrupole anisotropy of the background image, which can be observed from ellipticities of background galaxy images (Kaiser et al. 1995). The local area distortion due to gravitational lensing, or magnification, is given by the inverse Jacobian determinant,

$$\mu = \frac{1}{\det \mathcal{A}} = \frac{1}{(1 - \kappa)^2 - |\gamma|^2}, \quad (2)$$

where we assume subcritical lensing, i.e., $\det \mathcal{A}(\theta) > 0$. The lens magnification μ can be measured from characteristic variations in the number density of background galaxies (Broadhurst et al. 1995, see also § 3.2).

The lensing convergence κ is a weighted projection of the matter density contrast along the line of sight (e.g., Jain et al. 2000). For gravitational lensing in the cluster regime (e.g., Umetsu 2010), κ is expressed as $\kappa(\theta) = \Sigma_{\text{crit}}^{-1} \Sigma(\theta)$, namely the projected mass density $\Sigma(\theta)$ in units of the critical surface mass density for gravitational lensing, defined as

$$\Sigma_{\text{crit}} = \frac{c^2}{4\pi G D_d} \langle \beta \rangle^{-1}; \quad \beta(z_s) \equiv \max \left[0, \frac{D_{ds}(z_s)}{D_s(z_s)} \right], \quad (3)$$

where D_s , D_d , and D_{ds} are the proper angular diameter distances from the observer to the source, from the observer to the deflecting lens, and from the lens to the source, respectively, and $\langle \beta \rangle = \langle D_{ds}/D_s \rangle$ is the mean distance ratio averaged over the population of source galaxies in the cluster field.

In general, the observable quantity for quadrupole weak lensing is not the gravitational shear γ but the complex *reduced* shear (see § 3.1),

$$g(\theta) = \frac{\gamma(\theta)}{1 - \kappa(\theta)} \quad (4)$$

in the subcritical regime where $\det \mathcal{A} > 0$ (or $1/g^*$ in the negative parity region with $\det \mathcal{A} < 0$). The re-

duced shear g is invariant under the following global linear transformation:

$$\kappa(\theta) \rightarrow \lambda \kappa(\theta) + 1 - \lambda, \quad \gamma(\theta) \rightarrow \lambda \gamma(\theta) \quad (5)$$

with an arbitrary scalar constant $\lambda \neq 0$ (Schneider & Seitz 1995). This transformation is equivalent to scaling the Jacobian matrix $\mathcal{A}(\theta)$ with λ , $\mathcal{A}(\theta) \rightarrow \lambda \mathcal{A}(\theta)$, and hence leaves the critical curves $\det \mathcal{A}(\theta) = 0$ invariant. Furthermore, the curve $\kappa(\theta) = 1$, on which the gravitational distortions disappear, is left invariant under the transformation (5).

This mass-sheet degeneracy can be unambiguously broken by measuring the magnification effects (see § 3.2), because the magnification μ transforms under the invariance transformation (5) as

$$\mu(\theta) \rightarrow \lambda^2 \mu(\theta). \quad (6)$$

Alternatively, the constant λ can be determined such that the mean κ averaged over the outermost cluster region vanishes, if a sufficiently wide sky coverage is available.¹⁰

3. CLUSTER WEAK LENSING METHODOLOGY

In this section we develop a Bayesian method to reconstruct the projected cluster mass profile $\Sigma(\theta)$ from observable lens distortion and magnification profiles, without assuming particular functional forms for the mass distribution, i.e., in a model-independent fashion. Although the methodology here is presented for the analysis of individual clusters, it can be readily generalized for a statistical analysis using stacked lensing profiles of a sample of clusters. In § 4.6, alternatively, we provide a method to stack reconstructed projected mass profiles of individual clusters to obtain an ensemble-averaged profile.

3.1. Lens Distortion Profile

The observable quadrupole distortion of an object due to gravitational lensing is described by the spin-2 reduced shear, $g = g_1 + ig_2$ (equation [4]), which is coordinate dependent. For a given cluster center on the sky, one can form coordinate-independent quantities, the tangential distortion g_+ and the 45° rotated component, from linear combinations of the distortion coefficients as $g_+ = -(g_1 \cos 2\phi + g_2 \sin 2\phi)$ and $g_\times = -(g_2 \cos 2\phi - g_1 \sin 2\phi)$, with ϕ being the position angle of an object with respect to the cluster center. In the strict weak-lensing limit, the azimuthally-averaged tangential distortion profile $g_+ \approx \gamma_+$ satisfies the following identity (e.g., Bartelmann & Schneider 2001): $\gamma_+(\theta) = \bar{\kappa}(<\theta) - \kappa(\theta)$, where $\kappa(\theta)$ is the azimuthal average of $\kappa(\theta)$ at radius θ , and $\bar{\kappa}(<\theta)$ is the mean convergence interior to radius θ . With the assumption of quasi-circular symmetry in the projected mass distribution (see Umetsu & Broadhurst 2008), the tangential distortion is expressed as

$$g_+(\theta) = \frac{\bar{\kappa}(<\theta) - \kappa(\theta)}{1 - \kappa(\theta)} \quad (7)$$

⁹ Throughout the paper we assume in our weak lensing analysis that the angular size of background galaxy images is sufficiently small compared to the scale over which the underlying lensing fields vary, so that the higher-order weak lensing effects, such as *flexion*, can be safely neglected; see, e.g., Goldberg & Bacon (2005); Okura et al. (2007, 2008).

¹⁰ Or, one may constrain the constant λ such that the enclosed mass within a certain aperture is consistent with cluster mass estimates from some other observations (e.g., Umetsu & Futamase 2000).

in the nonlinear but subcritical ($\det \mathcal{A}(\boldsymbol{\theta}) > 0$) regime.¹¹ In the absence of higher order effects, weak lensing only induces curl-free tangential distortions, while the azimuthal averaged \times component is expected to vanish. In practice, the presence of \times modes can be used to check for systematic errors.

From shape measurements of background galaxies, we calculate the weighted average of g_+ in a set of N radial bands ($i = 1, 2, \dots, N$) as

$$g_+(\bar{\theta}_i) = \left(\sum_{k \in i} w_{(k)} \right)^{-1} \left(\sum_{k \in i} w_{(k)} g_{+(k)} \right), \quad (8)$$

where $\bar{\theta}_i$ is the center of the i th radial band of $[\theta_i, \theta_{i+1}]$, the index k runs over all of the objects located within the i th annulus, $g_{+(k)}$ is the tangential distortion of the k th object, and $w_{(k)}$ is the statistical weight (see Umetsu & Broadhurst 2008; Umetsu et al. 2009, 2010) for the k th object, given by

$$w_{(k)} = \frac{1}{\sigma_{g(k)}^2 + \alpha_g^2} \quad (9)$$

with $\sigma_{g(k)}^2$ being the variance for the shear estimate of the k th galaxy and α_g^2 being the softening constant variance (e.g., Hamana et al. 2003). In our analysis, we choose $\alpha_g = 0.4$, which is a typical value of the mean rms σ_g over the background sample (e.g., Hamana et al. 2003; Umetsu & Broadhurst 2008; Umetsu et al. 2009, 2010). We use the continuous limit of the area-weighted band center for $\bar{\theta}_i$ (see equation [B3]). We perform a bootstrap error analysis to assess the uncertainty $\sigma_+(\theta)$ in the tangential distortion profile $g_+(\theta)$.

3.2. Magnification Bias Profile

Lensing magnification, $\mu(\boldsymbol{\theta})$, influences the observed surface density of background sources, expanding the area of sky, and enhancing the observed flux of background sources (Broadhurst et al. 1995). The former effect reduces the effective observing area in the source plane, decreasing the number of background sources per solid angle; on the other hand, the latter effect amplifies the flux of background sources, increasing the number of sources above the limiting flux. The net effect is known as magnification bias, and depends on the intrinsic slope of the luminosity function of background sources.

The number counts for a given magnitude cutoff m_{cut} , approximated locally as a power-law cut with slope $s = d \log_{10} N(< m) / dm$ ($s > 0$), are modified in the presence of lensing as

$$N(< m_{\text{cut}}) \approx N_0(< m_{\text{cut}}) \mu^{2.5s-1} \quad (10)$$

(Broadhurst et al. 1995), where $N_0(< m_{\text{cut}})$ is the unlensed counts, and μ is the magnification, $\mu = (1 - \kappa)^{-2}(1 - |g|^2)^{-1}$. In the strict weak lensing limit, the magnification bias is $\delta N/N_0 \approx (5s - 2)\kappa$.

¹¹ In general, a wide spread of the redshift distribution of background galaxies, in conjunction with the single-plane approximation, may lead to an overestimate of the gravitational shear in the nonlinear regime (Hoekstra et al. 2000). Thanks to the deep Subaru photometry, we found that this bias in the observed reduced shear is approximately $\Delta g/g \sim 0.02\kappa$ to the first order of κ . See § 3.4 of Umetsu et al. (2010) for details.

For the number counts to measure magnification, we use a sample of *red* background galaxies, for which the intrinsic count slope s at faint magnitudes is relatively flat, $s \sim 0.1$, so that a net count depletion results (Broadhurst et al. 2005a; Umetsu & Broadhurst 2008; Umetsu et al. 2010). On the other hand, the faint blue background population tends to have a steeper intrinsic count slope close to the lensing invariant slope ($s = 0.4$). The count-in-cell statistic $N(\boldsymbol{\theta}; < m_{\text{cut}})$ is measured from a flux-limited sample of red background galaxies on a regular grid of equal-area cells, each with a solid angle of $\Delta\Omega = (\Delta\theta)^2$. Note that a practical difficulty of the magnification bias measurement is contamination due to the intrinsic clustering of background galaxies, which locally can be larger than the lensing-induced signal in a given cell. In order to obtain a clean measure of the lensing signal, such intrinsic clustering needs to be downweighted (e.g., Broadhurst et al. 1995; Zhang & Pen 2005).

For a mass profile analysis, we calculate the mean number density $n_\mu(\bar{\theta}_i) = dN(\bar{\theta}_i)/d\Omega$ of the red background sample as a function of radius from the cluster center, by azimuthally averaging $N(\boldsymbol{\theta})$, using the same radial bins ($i = 1, 2, \dots, N$) as done for the distortion measurement. The lens magnification bias is expressed in terms of the number density of background galaxies as $n_\mu(\theta) = n_0\mu(\theta)^{2.5s-1}$ with n_0 being the unlensed mean surface number density of background galaxies. The normalization and slope parameters (n_0, s) can be estimated from the source counts in cluster outskirts using wide-field imaging data (§4.2). In practice, we adopt the following prescription:

- A positive tail of $> 3\sigma$ cells is excluded in each annulus to remove inherent small scale clustering of the background (Broadhurst et al. 2008).
- Each grid cell is weighted by the fraction of its area lying within the respective annular bins (Marshall et al. 2002; Umetsu & Broadhurst 2008).
- The uncertainty $\sigma_\mu(\theta)$ in $n_\mu(\theta)$ includes not only the Poisson contribution but also the variance due to variations of the counts along the azimuthal direction, i.e., contributions from the intrinsic clustering of background galaxies (Umetsu et al. 2010).
- The cell size $\Delta\theta$ can be as large as the typical radial band width for a mass profile analysis, which can cause an additional variance due to Poisson and sampling errors. We thus average over a set of radial profiles obtained using different grids offset with respect to each other by half a grid spacing in each direction.
- The masking effect due to bright cluster galaxies, bright foreground objects, and saturated pixels is properly taken into account and corrected for (Umetsu & Broadhurst 2008). In our analysis, we use Method B of Appendix A developed in this work.

3.3. Bayesian Mass Profile Reconstruction

The relation between distortion and convergence is nonlocal, and the convergence derived from distortion data alone suffers from a mass-sheet degeneracy (§ 2). However, by combining the distortion and magnification measurements the convergence can be obtained unambiguously with the correct mass normalization. Here we aim to derive a discrete convergence profile from observable lens distortion and magnification profiles (see § 3.1 and § 3.2) within a Bayesian statistical framework, allowing for a full parameter-space extraction of model and calibration parameters. A proper Bayesian statistical analysis is of particular importance to explore the entire parameter space and investigate the parameter degeneracies, arising in part from the mass-sheet degeneracy.

In this framework, we sample from the posterior probability density function (PDF) of the underlying signal \mathbf{s} given the data \mathbf{d} , $P(\mathbf{s}|\mathbf{d})$. Expectation values of any statistic of the signal \mathbf{s} shall converge to the expectation values of the a posteriori marginalized PDF, $P(\mathbf{s}|\mathbf{d})$. In our problem, the signal \mathbf{s} is a vector containing the discrete convergence profile, $\kappa_i \equiv \kappa(\bar{\theta}_i)$ ($i = 1, 2, \dots, N$), and the average convergence within the inner radial boundary $\theta_{\min} \equiv \theta_1$ of the weak lensing data, $\bar{\kappa}_{\min} \equiv \bar{\kappa}(< \theta_{\min})$, so that $\mathbf{s} = \{\bar{\kappa}_{\min}, \kappa_1, \kappa_2, \dots, \kappa_N\}$, being specified by $(N+1)$ parameters. The Bayes' theorem states that

$$P(\mathbf{s}|\mathbf{d}) \propto P(\mathbf{s})P(\mathbf{d}|\mathbf{s}), \quad (11)$$

where $\mathcal{L}(\mathbf{s}) \equiv P(\mathbf{d}|\mathbf{s})$ is the likelihood of the data given the model (\mathbf{s}), and $P(\mathbf{s})$ is the prior probability distribution for the model parameters.

3.3.1. Weak Lensing Likelihood Function

We combine complementary and independent weak lensing information of tangential distortion and magnification bias to constrain the underlying cluster mass distribution $\mathbf{s} = \{\bar{\kappa}_{\min}, \kappa_i\}_{i=1}^N$. The total likelihood function \mathcal{L} of the model \mathbf{s} for combined weak lensing observations is given as a product of the two separate likelihoods, $\mathcal{L} = \mathcal{L}_g \mathcal{L}_\mu$, where \mathcal{L}_g and \mathcal{L}_μ are the likelihood functions for distortion and magnification, respectively. The log-likelihood for the tangential distortion is given as

$$-\ln \mathcal{L}_g = \frac{1}{2} \sum_{i=1}^N \frac{[g_{+,i} - \hat{g}_{+,i}(\mathbf{s})]^2}{\sigma_{+,i}^2} + \text{const.}, \quad (12)$$

where $\hat{g}_{+,i}(\mathbf{s})$ is the theoretical prediction for the observed distortion $g_{+,i}$, and the errors $\sigma_{+,i}$ ($i = 1, 2, \dots, N$) due primarily to the variance of the intrinsic source ellipticity distribution can be conservatively estimated from the data using Bootstrap techniques (§ 3.1). Similarly, the log-likelihood function for the magnification bias is given as

$$-\ln \mathcal{L}_\mu = \frac{1}{2} \sum_{i=1}^N \frac{[n_{\mu,i} - \hat{n}_{\mu,i}(\mathbf{s})]^2}{\sigma_{\mu,i}^2} + \text{const.}, \quad (13)$$

where $\hat{n}_{\mu,i}(\mathbf{s})$ is the theoretical prediction for the observed counts $n_{\mu,i}$, and the errors $\sigma_{\mu,i}$ include both contributions from Poisson errors in the counts, $\sigma_{\text{Poisson},i}$, and contamination due to intrinsic clustering of red back-

Table 1
The Cluster Sample: Redshift and Subaru Filter Information

Cluster	Redshift	Filters	Detection band	Seeing ^a (arcsec)	Refs.
A1689	0.183	$i'V$	i'	0.82	1
A1703	0.281	$g'r'i'$	r'	0.78	2,3
A370	0.375	$B_j R_c z'$	R_c	0.60	2,3
Cl0024+17	0.395	$B_j R_c z'$	R_c	0.80	4
RXJ1347-11	0.451	$V R_c z'$	R_c	0.76	2,3

References. — [1] Umetsu & Broadhurst (2008); [2] Broadhurst et al. (2008); [3] Medezinski et al. (2010); [4] Umetsu et al. (2010).

Note. — For observational details, see the references. Refs. [2] and [3] adopted a cluster redshift of $z = 0.258$ for A1703.

^a Seeing FWHM in units of arcsec in the final co-added detection image.

Table 2
Einstein Radius Information

Cluster	Einstein radius, θ_{ein} (arcsec)	Refs.
A1689	$53 \pm 3''$ ($z_s = 3.04$) ^a	1,2
A1703	$31 \pm 3''$ ($z_s = 2.627$)	3, 4, 5
A370	$37 \pm 3''$ ($z_s = 2$)	6, 7
Cl0024+17	$30 \pm 3''$ ($z_s = 1.675$)	8
RXJ1347-11	$35 \pm 2''$ ($z_s = 2.2$)	7, 9, 10

References. — [1] Broadhurst et al. (2005b); [2] Coe et al. (2010); [3] Limousin et al. (2008); [4] Richard et al. (2009); [5] Zitrin et al. (2010); [6] Richard et al. (2010); [7] Zitrin et al. (2011), in preparation; [8] Zitrin et al. (2009); [9] Halkola et al. (2008); [10] Bradač et al. (2008).

^a This Einstein radius constraint translates into $\theta_{\text{ein}} \simeq 47''$ at $z_s = 2$ (cf. $\theta_{\text{ein}} = 47.0 \pm 1.2''$ at $z_s = 2$ by Ref. [2]).

ground galaxies, $\sigma_{\text{clust},i}$, as discussed in § 3.2:

$$\sigma_{\mu,i}^2 = \sigma_{\text{Poisson},i}^2 + \sigma_{\text{clust},i}^2. \quad (14)$$

The lensing observables $g_{+,i}$ and $n_{\mu,i}$ ($i = 1, 2, \dots, N$) can be readily expressed by the given model parameters \mathbf{s} , as shown in Appendices B and C.

3.3.2. Prior Information

For each parameter of the model \mathbf{s} , we consider a simple flat prior with a lower bound of $\mathbf{s} = 0$, that is,

$$\bar{\kappa}_{\min} > 0, \quad (15)$$

$$\kappa_i > 0 \quad (i = 1, 2, \dots, N). \quad (16)$$

Additionally, we account for the calibration uncertainty in the observational parameters, i.e., the normalization and slope parameters (n_0, s) of the background counts and the relative lensing depth ω due to population-to-population variations between the background samples used for the magnification and distortion measurements (see Appendix C).

4. APPLICATIONS: SUBARU OBSERVATIONS OF FIVE STRONG-LENSING CLUSTERS

4.1. Cluster Sample and Observations

Table 3
Background galaxy samples

Cluster	Distortion analysis (full background)			Magnification analysis (red background)			ω^d
	\bar{n}^a (arcmin $^{-2}$)	$\bar{z}_{s,\beta}^b$	$\langle\beta\rangle^c$	\bar{n} (arcmin $^{-2}$)	$\bar{z}_{s,\beta}$	$\langle\beta\rangle$	
A1689 ^a	8.8	0.71 ± 0.12	0.69	12.0	0.71 ± 0.12	0.69	1.00
A1703	10.0	1.10 ± 0.18	0.68	6.9	0.93 ± 0.12	0.64	0.95
A370 ^b	16.7	1.11 ± 0.12	0.58	21.6	1.05 ± 0.11	0.57	0.98
Cl0024+17	17.2	1.29 ± 0.15	0.61	17.8	1.14 ± 0.09	0.56	0.92
RXJ1347-11	6.4	0.98 ± 0.06	0.47	7.7	1.04 ± 0.07	0.49	1.05

Note. — We assume 5% uncertainty in our estimates of the relative lensing depth ω .

^a Mean surface number density of background galaxies.

^b Effective mean source redshift of the background sample corresponding to the mean depth $\langle\beta\rangle$, defined such that $\beta(\bar{z}_{s,\beta}) = \langle\beta\rangle$.

^c Distance ratio averaged over the redshift distribution of the background sample, taken from Umetsu & Broadhurst (2008, A1689), Medezinski et al. (2010, A1703, A370, RXJ1347-11) and Umetsu et al. (2010, Cl0024+17).

^d Relative lensing depth of the red background sample, $\omega = \langle\beta(\text{red})\rangle/\langle\beta(\text{full})\rangle$, with respect to the full background sample.

Table 4
Normalization and slope of red background counts

Cluster	m_{cut}^a (AB mag)	Normalization, n_0^b (arcmin $^{-2}$)	Slope, s^c
A1689	$i' = 25.5$	11.5 ± 0.3	0.124 ± 0.060
A1703	$i' = 26$	8.2 ± 0.2	0.099 ± 0.070
A370	$z' = 26$	22.5 ± 0.4	0.042 ± 0.070
Cl0024+17	$z' = 25.5$	18.3 ± 0.3	0.121 ± 0.040
RXJ1347-11	$z' = 26$	7.0 ± 0.3	0.025 ± 0.070

^a Fainter magnitude cut of the red background sample, m_{cut} .

^b Normalization of unlensed red background counts, n_0 .

^c Slope of the unlensed red background counts at m_{cut} , $s = d \log_{10} N_0(< m_{\text{cut}})/dm$.

In this section we apply our Bayesian mass reconstruction method to a sample of five well-studied high-mass clusters ($M \gtrsim 10^{15} M_\odot$) at intermediate redshifts, A1689 ($z = 0.183$), A1703 ($z = 0.281$), A370 ($z = 0.375$), Cl0024+17 ($z = 0.395$), and RXJ1347-11 ($z = 0.451$), observed with the wide-field camera ($34'' \times 27''$; see Miyazaki et al. 2002) on the 8.2m Subaru telescope. Table 1 gives a summary of cluster observations. The clusters were observed deeply in several optical passbands, with exposures in the range 2000–10000s per passband, with seeing in the detection images ranging from $0.6''$ to $0.8''$ (see Umetsu & Broadhurst 2008; Broadhurst et al. 2008; Medezinski et al. 2010; Umetsu et al. 2010).

These massive clusters are known as strong lensing clusters, displaying prominent strong-lensing features and large Einstein radii of $\theta_{\text{ein}} \gtrsim 30''$ (e.g., for a fiducial source redshift $z_s \sim 2$; Broadhurst & Barkana 2008; Oguri & Blandford 2009). For the clusters, the central mass distributions have been recovered in detail by our strong-lens modeling (Broadhurst et al. 2005b; Zitrin et al. 2009, 2010). Here the models were constrained by a number of multiply-lensed images identified previously in very deep multi-color imaging with *HST*/ACS (e.g., Broadhurst et al. 2005b; Bradač et al. 2008; Halkola et al. 2008; Limousin et al. 2008; Richard et al. 2009, 2010; Zitrin et al. 2009, 2010). Table 2 gives a summary of the Einstein radii of the five clusters as constrained from our detailed strong lens

modeling with the ACS observations.

4.2. Background Galaxy Samples

Here we will add to our high-quality spin-2 shape measurements (Umetsu & Broadhurst 2008; Medezinski et al. 2010; Umetsu et al. 2010) the independent magnification information based on deep multi-band imaging with Subaru, in order to achieve the maximum possible lensing precision. Full details of the Subaru observations and weak-lensing shape analysis of these clusters were presented in a series of our papers (Umetsu & Broadhurst 2008; Broadhurst et al. 2008; Umetsu et al. 2009; Medezinski et al. 2010; Umetsu et al. 2010; Zitrin et al. 2010, see also Table 1). The level of shear calibration bias with our implementation of the KSB+ method (Kaiser et al. 1995) has been assessed by Umetsu et al. (2010) using simulated Subaru Suprime-Cam images (M. Oguri 2010, in private communication; Massey et al. 2007). We find, typically, $|m| \lesssim 5\%$ of the shear calibration bias, and $c \sim 10^{-3}$ of the residual shear offset which is about 1 order of magnitude smaller than the typical distortion signal in cluster outskirts. This level of calibration bias is subdominant compared to the statistical uncertainty ($\Delta M/M \sim 15\%$) due to the intrinsic scatter in galaxy shapes, and to the dilution effect which can lead to an underestimation of the true signal for $R \lesssim 400 \text{ kpc } h^{-1}$ by a factor of 2–5 (see Figure 1 of Broadhurst et al. 2005a).

A careful background selection is critical for a weak-lensing analysis so that unlensed cluster members and foreground galaxies do not dilute the true lensing signal of the background (Broadhurst et al. 2005a; Medezinski et al. 2007, 2010). We use undiluted samples of background galaxies derived in our previous lensing work, as summarized in Table 3. When deep multi-color photometry is available in our cluster fields, we use the background selection method of Medezinski et al. (2010, see also Umetsu et al. 2010) to define blue and red background samples (A1703, A370, Cl0024+17, RXJ1347-11), which relies on empirical correlations for galaxies in color-color space derived from the deep Subaru photometry, by reference to the deep photometric

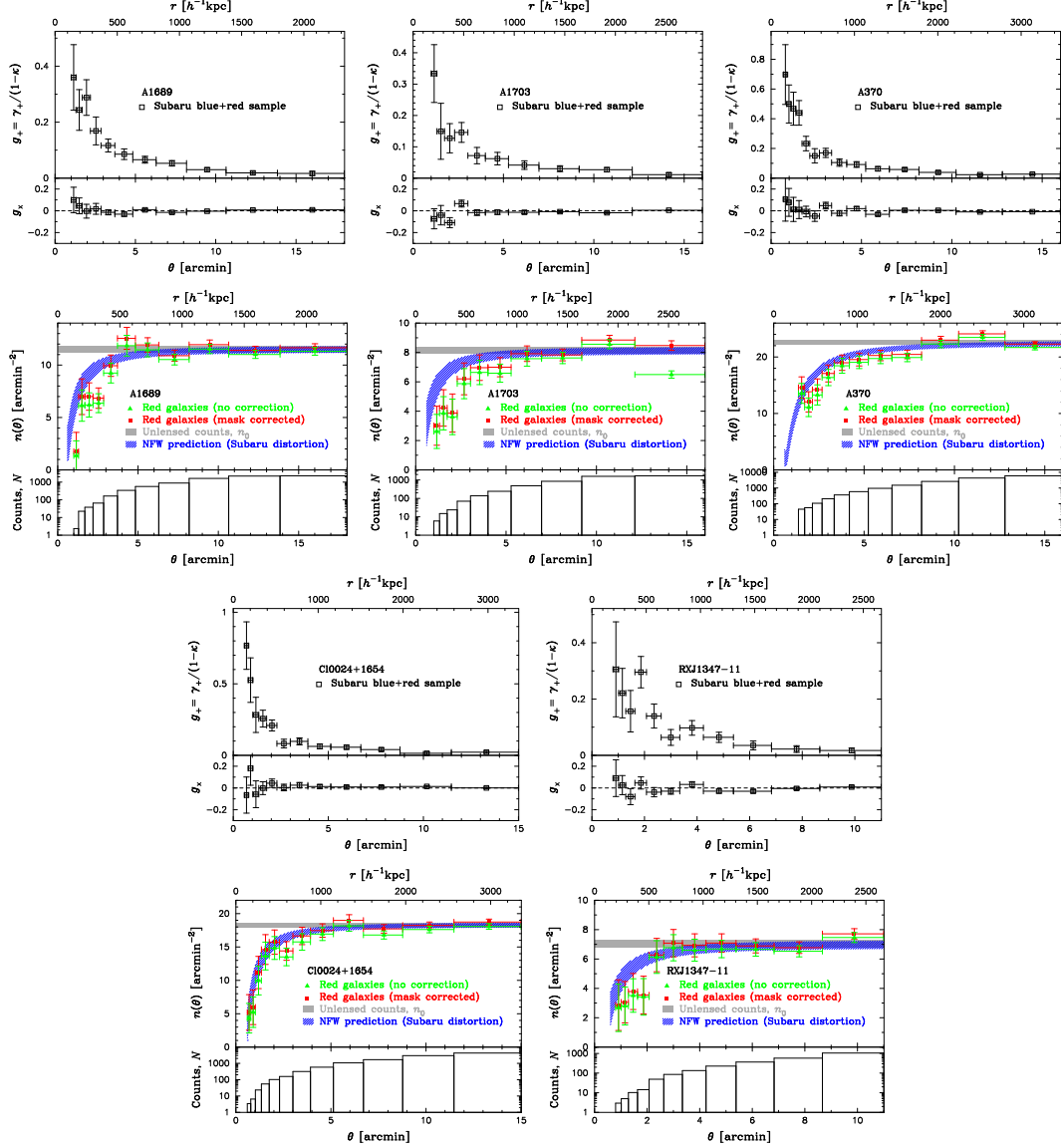


Figure 1. Radial profiles of the averaged spin-2 distortion and magnification bias measurements based on background galaxies registered in deep Subaru images, shown separately for the five clusters, A1689 (top-left), A1703 (top-middle), A370 (top-right), C10024+17 (bottom-left), and RXJ1347-11 (bottom-right). For each cluster, the top panels show the radial profiles (open squares and error bars) of the tangential distortion (upper panel) and the 45° rotated (×) component (lower panel) based on the spin-2 shape measurements of the full background galaxy sample (Table 3). The squares and triangles (upper panel) show the respective results with and without the mask correction due to bright foreground objects and cluster members. The blue hatched area represents the 68.3% confidence bounds for the predicted count depletion curve from an NFW model constrained by our Subaru distortion analysis, demonstrating clear consistency between these two independent lensing observables. The gray horizontal bar represents the constraints on the unlensed count normalization n_0 . The histogram in the lower panel shows the observed counts of the red background galaxies in each annular bin.

redshift survey in the COSMOS field (Ilbert et al. 2009). Otherwise, we use the color-magnitude selection method (Broadhurst et al. 2005a; Medezinski et al. 2007; Umetsu & Broadhurst 2008) to define a sample of red galaxies (A1689) whose colors are redder than the red sequence of cluster E/S0 galaxies. These red galaxies are expected to lie in the background by virtue of K -corrections which are greater than the red cluster sequence galaxies, as convincingly demonstrated spectroscopically by Rines & Geller (2008). Apparent magnitude cuts are applied in the reddest band available for each cluster to avoid incompleteness near the detection limit.

A flux-limited sample of red background galaxies is used for the magnification analysis (see § 3.2). For the distortion analysis, we use a full composite sample of red and blue (if available) background galaxies, where the galaxies used are well resolved to make reliable shape measurements (see, e.g., Umetsu et al. 2010). Table 3 lists for respective color samples the mean surface number density \bar{n} of background galaxies, the effective source redshift, $\bar{z}_{s,\beta}$,¹² and the mean distance r_a

¹² The effective single-lens plane redshift $\bar{z}_{s,D}$, corresponding to the mean depth $\langle\beta\rangle$, is defined as $\langle\beta\rangle = \beta(\bar{z}_{s,\beta})$. For details, see § 3.4 of Umetsu et al. (2010).

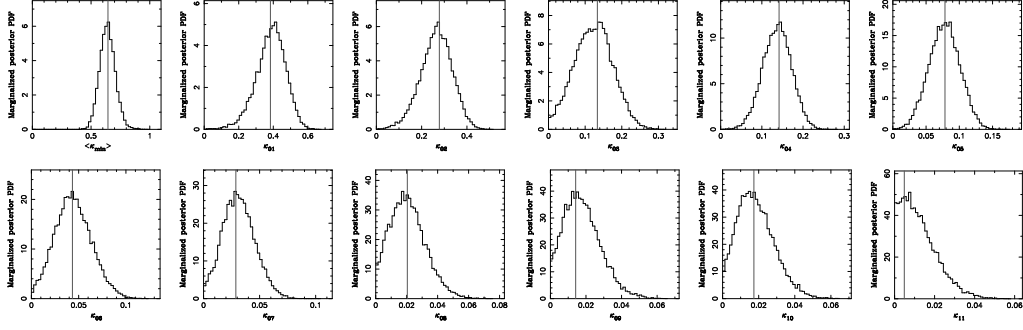


Figure 2. One-dimensional marginalized posterior probability density functions (PDFs) for the discrete mass profile $\mathbf{s} = (\kappa_{\min}, \kappa_1, \kappa_2, \dots, \kappa_N)$, shown for A1689 (see Figure 3). The solid vertical lines show the peak locations (mode values) of the a posteriori marginalized distribution for each parameter. The results are marginalized over all other parameters, including the observational parameters (n_0, s, ω) . The resulting posterior distributions are all single-peaked, and nearly Gaussian for most of the model parameters. The mass-sheet degeneracy is broken thanks to the inclusion of magnification data.

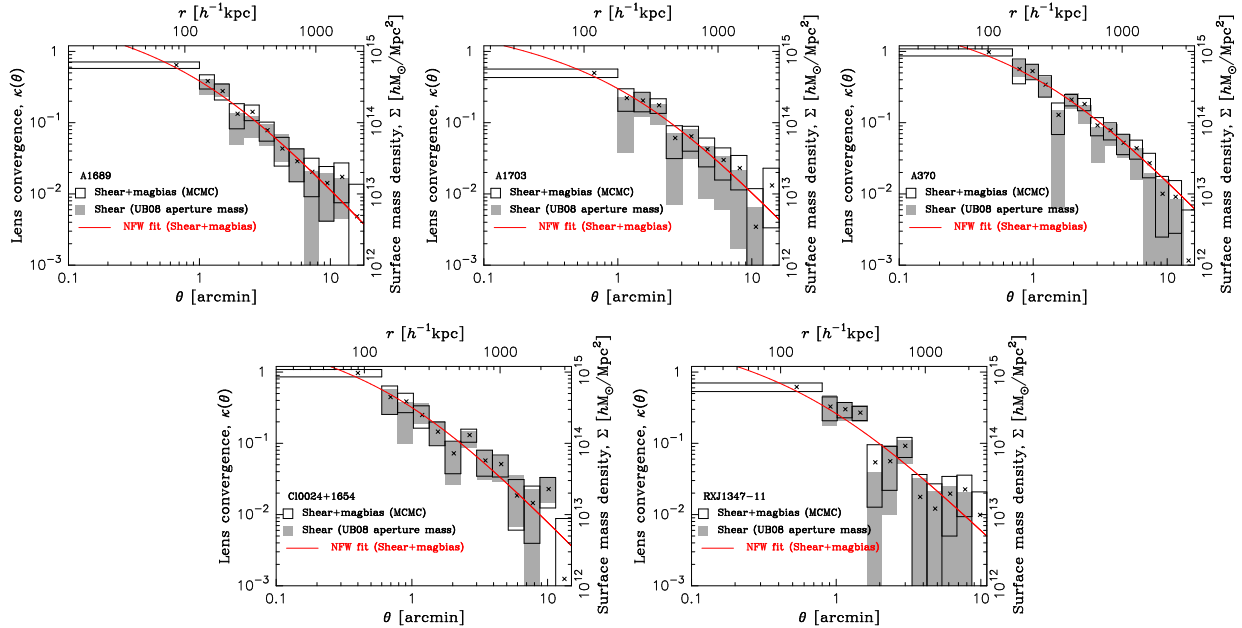


Figure 3. Reconstructed projected mass profiles $\kappa(\theta) = \Sigma(\theta)/\Sigma_{\text{crit}}$ for the five clusters, A1689 (top left), A1703 (top middle), A370 (top right), Cl0024+17 (bottom left), and RXJ1347-11 (bottom right). The open boxes show the results obtained using the Bayesian mass reconstruction method from the combined Subaru tangential distortion and magnification bias measurements of background galaxies (Figure 1). The innermost (first) box represents the average convergence $\bar{\kappa}(<\theta_{\min})$ interior to the minimum radius θ_{\min} of the weak lensing data. Also shown for each cluster is the best-fit NFW profile (solid curve) for the combined Subaru distortion and magnification data. The gray boxes represent the mass profile reconstructed using the nonlinear extension of aperture mass densitometry by Umetsu & Broadhurst (2008) based on the same tangential distortion data (but without the magnification data combined), which employs an outer boundary condition on the mean convergence in the outermost radial bin. The horizontal extent of each box represents the range of the radial band, and its vertical extent shows the statistical 1σ uncertainty in κ . The cross in each open box indicates the band-averaged convergence, being marked at the area-weighted center of the radial band. The errors are correlated in both reconstructions.

to $\langle\beta\rangle$ averaged over the source redshift distribution. We also quote in Table 3 the values of the relative mean depth, $\omega = \langle\beta(\text{red})\rangle/\langle\beta(\text{full})\rangle$, between the background samples used for the magnification and distortion measurements (see § 3.3.2 and Appendix C). We adopt a conservative uncertainty of 5% in the relative mean depth ω for all of the clusters based on our previous work (Umetsu & Broadhurst 2008; Umetsu et al. 2009; Medezinski et al. 2010; Umetsu et al. 2010).

The conversion from the observed counts into magnification depends on the normalization n_0 and the slope parameter s of the unlensed number counts, which can be reliably estimated thanks to the wide field of view

of Subaru/Suprime-Cam (see § 4.4). Table 4 lists the magnitude cuts (m_{cut}) and unlensed count parameters (n_0, s) as measured from the red background counts in outermost annular regions in cluster outskirts ($\gtrsim 10'$).

4.3. Subaru Weak Lensing Profiles

Following the methodology outlined in § 3.1 and § 3.2 (see also Appendix A), we derive lens distortion and magnification profiles of five massive clusters from Subaru observations. In order to obtain meaningful radial profiles, one must carefully define the center of the cluster. It is often assumed that the cluster mass centroid coincides with the position of the brightest cluster galaxy (BCG),

Table 5
Subaru weak lensing data

Cluster	$\theta_{\min}, \theta_{\max}$ ($''$)	N	Detection S/N		
			g_+	n_μ	Combined (κ)
A1689	1, 18	11	13.8	8.8	17.8
A1703	1, 16	10	9.9	7.1	12.7
A370	0.7, 16	14	17.3	11.0	23.8
Cl0024+17	0.6, 15	12	13.0	8.5	18.5
RXJ1347-11	0.8, 11	11	9.7	5.7	12.6

Note. — The lensing profiles are calculated in N discrete radial bins over the radial range of $\theta = [\theta_{\min}, \theta_{\max}]$, with a logarithmic radial spacing of $\Delta \ln \theta = \ln(\theta_{\max}/\theta_{\min})/N$. For each cluster, θ_{\min} is taken such that $\theta_{\min} > \theta_{\text{ein}}$ (see Table 2).

whereas the BCGs can be offset from the mass centroids of the corresponding dark matter halos (Johnston et al. 2007; Oguri et al. 2010; Oguri & Takada 2011). Here we utilize our detailed mass maps in the cluster cores recovered from strong-lens modeling of ACS observations (§4.1), providing an independent mass-centroid determination. We find that for these five clusters there is only a small offset of typically $\lesssim 5''$ (20 kpc h^{-1} at the highest cluster redshift of our study, $z_d = 0.451$) between the BCG and the dark-matter center of mass (see also § 4.2 of Umetsu et al. 2010), often implied by other massive bright galaxies in the vicinity of the BCG. This level of cluster centering offset is substantially small as compared to the typical inner radial boundary of weak lensing observations, $\theta_{\min} \sim 1'$. In the present work, we therefore simply assume that the cluster mass centroid coincides with the location of the BCG, which is adopted as the cluster center in our one-dimensional profile analysis.

The lensing profiles were calculated in N discrete radial bins over the range of radii $\theta = [\theta_{\min}, \theta_{\max}]$, with a constant logarithmic radial spacing of $\Delta \ln \theta = \ln(\theta_{\max}/\theta_{\min})/N$, where the inner radial boundary θ_{\min} is taken such that $\theta_{\min} > \theta_{\text{ein}}$ (see Table 2). The typical inner boundary is $\theta_{\min} \sim 1' (> \theta_{\text{ein}})$ for cluster weak lensing. The outer radial boundary θ_{\max} was chosen to be sufficiently larger than the typical virial radius of high mass clusters with $M_{\text{vir}} = (1-2) \times 10^{15} M_\odot h^{-1}$, $R_{\text{max}} = D_d \theta_{\max} \gtrsim 3$ Mpc, but sufficiently small ($\theta_{\max} \lesssim 18'$) with respect to the size of the Suprime-Cam’s field-of-view so as to ensure accurate PSF (point spread function) anisotropy correction. The number of radial bins N was determined for each cluster such that the per-pixel detection signal-to-noise ratio (S/N) is of the order of unity,¹³ which is optimal for an inversion problem. The radial binning scheme is summarized in Table 5.

In Figure 1 we show the resulting distortion and magnification profiles for our sample of five massive lensing clusters. In all the clusters, a strong depletion of the red galaxy counts is seen in the central, high-density region of the cluster, and clearly detected out to several arcminutes from the cluster center. The statistical significance of the detection of the depletion signal is in the range 6σ – 11σ (see Table 5). The detection significance of the tangential distortion derived from the full background sample ranges from 10σ to 17σ , and is better than the red counts (see, e.g., Bartelmann & Schneider 1999). The \times -component is consistent with a null signal

¹³ We quantify the significance of a detection for a given lensing profile in analogy to equation (38) of Umetsu & Broadhurst (2008).

in most of radial bins, indicating the reliability of our weak-lensing analysis. The magnification measurements with and without the masking correction are roughly consistent with each other. Typically, the masking area is negligible (a few %) at large radii, and increases up to (10 – 20)% of the sky close to the cluster center (see Appendix A). To test the consistency between our distortion and depletion measurements, we calculate the depletion of the counts expected for the best-fitting NFW profile derived from the distortion measurements (Figure 1), normalized to the observed density n_0 (Table 4). This comparison shows clear consistency between two independent lensing observables with different systematics (see § 5.5 of Umetsu & Broadhurst 2008), which strongly supports the reliability and accuracy of our weak-lensing analysis (see also supplemental material presented in Appendix D).

4.4. Cluster Mass Profile Reconstruction

We use a Markov chain Monte Carlo (MCMC) approach with Metropolis-Hastings sampling to reconstruct the discrete cluster mass profile $\mathbf{s} = \{\bar{\kappa}_{\min}, \kappa_i\}_{i=1}^N$ within a Bayesian statistical framework (§ 3.3). We largely follow the sampling procedure outlined in Dunkley et al. (2005), but employ the Gelman-Rubin R statistic (Gelman & Rubin 1992) as a simple but reasonable convergence criterion of generated chains. Once convergence to a stationary distribution is achieved, we run a long final chain of 300,000 steps, which adequately samples the underlying posterior probability distribution. For all of the parameters, the number of iterations required for convergence is much less than our final chain length. Note, only the final chain is used for our parameter estimations and error analysis. We estimate the location of the maximum a posteriori probability for each model parameter using the bisection method in conjunction with bootstrap techniques. The covariance matrix C_{ij} ($i, j = 1, 2, \dots, N+1$) for the discrete mass profile \mathbf{s} is estimated from the MCMC samples. As an example, we show in Figure 2 one-dimensional marginalized posterior PDFs for the mass profile \mathbf{s} of A1689 ($N = 11$). The results are marginalized over all other parameters, including the observational parameters (n_0, s, ω).

The resulting posterior distributions are all clearly single-peaked, and approximately Gaussian for most of the parameters. It is clearly evident that the mass-sheet degeneracy is broken thanks to the inclusion of magnification information on the local area distortion. Excluding magnification data, on the other hand, strongly modifies the Gaussian shape of the marginalized posterior PDFs, producing long non-Gaussian tails and broadening the distribution function, resulting in large errors for the reconstructed mass profile. The improvement here from adding the magnification measurements is significant, $\sim 30\%$ in terms of cluster mass profile measurements (see Table 5).

Figure 3 shows the lensing convergence profiles $\mathbf{s} = \{\bar{\kappa}_{\min}, \kappa_1, \kappa_2, \dots, \kappa_N\}$, for the five clusters reconstructed using our Bayesian method from combined Subaru distortion and magnification data. Also shown for comparison are independent reconstructions from the same tangential distortion data (but without the magnification data combined) using the one-dimensional method of Umetsu & Broadhurst (2008, see also Umetsu et al.

Table 6
Best-fit NFW model parameters

Cluster	NFW (weak lensing)				gNFW (weak+strong lensing)				
	M_{vir} ($10^{15} M_{\odot} h^{-1}$)	c_{vir}	χ^2/dof	$\theta_{\text{ein}}^{\text{a}}$ ($''$)	M_{vir} ($10^{15} M_{\odot} h^{-1}$)	c_{-2}^{b}	α	χ^2/dof	$\theta_{\text{ein}}^{\text{a}}$ ($''$)
A1689	$1.282^{+0.217}_{-0.176}$	$12.80^{+3.09}_{-2.41}$	4.2/10	$48.7^{+15.6}_{-13.8}$	$1.301^{+0.193}_{-0.156}$	$13.71^{+1.19}_{-1.22}$	$0.268^{+0.415}_{-0.268}$	4.4/20	$49.7^{+12.9}_{-9.2}$
A1703	$1.232^{+0.244}_{-0.204}$	$7.02^{+2.36}_{-1.70}$	6.1/9	$28.1^{+16.3}_{-13.2}$	$1.272^{+0.234}_{-0.191}$	$7.07^{+1.08}_{-1.06}$	$0.934^{+0.192}_{-0.253}$	7.2/21	$27.9^{+14.7}_{-14.0}$
A370	$2.451^{+0.309}_{-0.262}$	$7.00^{+1.09}_{-0.92}$	10.2/13	$50.4^{+11.0}_{-10.0}$	$2.276^{+0.255}_{-0.220}$	$5.68^{+0.48}_{-0.48}$	$0.392^{+0.158}_{-0.190}$	15.2/26	$30.5^{+9.4}_{-10.7}$
Cl0024+17	$1.376^{+0.232}_{-0.201}$	$8.82^{+2.25}_{-1.68}$	11.7/11	$36.9^{+11.3}_{-10.1}$	$1.339^{+0.247}_{-0.203}$	$8.05^{+1.24}_{-1.28}$	$0.814^{+0.396}_{-0.717}$	11.1/23	$31.3^{+13.4}_{-9.2}$
RXJ1347-11	$1.488^{+0.277}_{-0.244}$	$9.08^{+3.14}_{-2.17}$	10.4/10	$43.2^{+13.6}_{-12.6}$	$1.435^{+0.114}_{-0.100}$	$7.16^{+0.43}_{-0.43}$	$0.046^{+0.205}_{-0.046}$	58.2/28	$32.4^{+5.1}_{-5.2}$

^a Einstein radius predicted by the best-fit NFW (gNFW) model, evaluated at the arc redshift given in Table 2.

^b Effective concentration parameter for gNFW, $c_{-2} \equiv r_{\text{vir}}/r_{-2} = c_{\text{vir}}/(2 - \alpha)$.

2010) based on the nonlinear extension of aperture mass densitometry, which employs an outer boundary condition on the mean convergence in the outermost radial bin, $\bar{\kappa}_{\text{max}} \equiv \bar{\kappa}(\theta_{N-1}, \theta_{\text{max}})$. Here $\bar{\kappa}_{\text{max}}$ for an isolated NFW halo can be negligibly small if the outermost radii are taken as large as the cluster virial radius (see Umetsu et al. 2010). This method has been applied successfully to Subaru weak lensing observations of massive clusters including A1689 (Umetsu & Broadhurst 2008; Umetsu et al. 2009), A1703 (Oguri et al. 2009; Zitrin et al. 2010), and Cl0024+17 (Umetsu et al. 2010). Our results with different combinations of lensing measurements and boundary conditions, having different systematics, are in agreement with each other. This consistency clearly demonstrates that our results are robust and insensitive to the choice of boundary condition as well as to systematic errors in the lensing measurements, such as the shear calibration error, as found by Umetsu & Broadhurst (2008).

Unlike the distortion effect, the magnification bias due to the local area distortion falls off sharply with increasing distance from the cluster center. We find from the reconstructed mass profiles that the lens convergence at large radii of $\theta = [10', 15']$ is of the order $\kappa = 5 \times 10^{-3} - 0.01$. The expected level of the depletion signal in the weak-lensing limit is $\delta n_{\mu}/n_0 \approx -2\kappa$ for a *maximally*-depleted sample with $s = 0$, indicating a depletion signal of $\lesssim (1 - 2)\%$ in the cluster outskirts where we have estimated the unlensed background counts, n_0 . This level of signal is smaller than the fractional uncertainties in estimated unlensed counts n_0 of $(2 - 4)\%$, thus consistent with the assumption. Note that the calibration uncertainties in our observational parameters (n_0, s, ω) have been properly taken into account and marginalized over in our Bayesian analysis.

In the presence of magnification, one probes the number counts at an effectively fainter limiting magnitude: $m_{\text{cut}} + 2.5 \log_{10} \mu(\theta)$. The level of magnification is on average small in the weak-lensing regime but for the innermost bin reaches a factor of 2 to 4 depending on the cluster. Here we use the count slope at the fainter effective limit (m_{lim}) when making the magnification estimate, to be self-consistent. In our analysis we have implicitly assumed that the power-law behavior (equation [10]) persists down to ~ 1 mag fainter than m_{cut} where the count slope may be shallower. For a given level of count depletion, an overestimation of the count slope could lead to an overestimation of the magnification, thus biasing the resulting mass profile. However,

the number count slope for our data flattens only slowly with depth varying from $s \sim 0.1$ to $s \sim 0.05$ from a limit of $m = 25.5$ to $m = 26.5$, so that this introduces a small correction of only typically 8%–11% for the most magnified bins ($\mu = 2 - 4$). In fact, we have found a good consistency between the purely shear-based results and the results based on the combined distortion and magnification data (see Figure 3).

To quantify and characterize the cluster mass distribution, we compare the reconstructed κ profile with the physically and observationally motivated NFW model. Here we consider a generalized parametrization of the NFW model of the following form (Zhao 1996; Jing & Suto 2000):

$$\rho(r) = \frac{\rho_s}{(r/r_s)^\alpha (1 + r/r_s)^{3-\alpha}}, \quad (17)$$

which has an arbitrary power-law shaped central cusp, $\gamma_{3D} = -\alpha$, and an asymptotic outer slope of $\gamma_{3D} = -3$. This reduces to the NFW model for $\alpha = 1$. We refer to the profile given by equation (17) as the generalized NFW (gNFW, hereafter) profile. It is useful to introduce the radius r_{-2} at which the logarithmic slope of the density is isothermal, i.e., $\gamma_{3D} = -2$. For the gNFW profile, $r_{-2} = (2 - \alpha)r_s$, and thus the corresponding concentration parameter reduces to $c_{-2} \equiv r_{\text{vir}}/r_{-2} = c_{\text{vir}}/(2 - \alpha)$. We specify the gNFW model with the central cusp slope, α , the halo virial mass, M_{vir} , and the concentration, $c_{-2} = c_{\text{vir}}/(2 - \alpha)$. We employ the radial dependence of the gNFW lensing profiles given by Keeton (2001).

We first fix the central cusp slope to $\alpha = 1$ (NFW), and constrain $(M_{\text{vir}}, c_{\text{vir}})$ from χ^2 fitting to the discrete cluster mass profile $\mathbf{s} = \{\bar{\kappa}_{\text{min}}, \kappa_i\}_{i=1}^N$ reconstructed from the combined weak-lensing distortion and magnification measurements. The χ^2 function for weak lensing is defined by

$$\chi^2 = \sum_{i=1}^{N+1} \sum_{j=1}^{N+1} [s_i - \hat{s}_i(M_{\text{vir}}, c_{\text{vir}})] C_{ij}^{-1} [s_j - \hat{s}_j(M_{\text{vir}}, c_{\text{vir}})], \quad (18)$$

where $\hat{\mathbf{s}}(M_{\text{vir}}, c_{\text{vir}})$ is the NFW model prediction for the discrete mass profile \mathbf{s} . The resulting constraints on the NFW model parameters and the predicted Einstein radius θ_{ein} are shown in Table 6. For all the cases, the best-fit NFW model from weak lensing properly reproduces the observed location of the Einstein radius, consistent with the independent strong-lensing observations (see Table 2). In Table 5 we quote the values of the total

detection S/N in the reconstructed mass profile \mathbf{s} based on the combined distortion and magnification data.

4.5. Cluster Mass Estimates

Our comprehensive Bayesian analysis of the weak lensing distortion and magnification of background galaxies allows us to recover the mass normalization, given as the mean convergence $\bar{\kappa}_{\min}$ within the innermost measurement radius θ_{\min} ($> \theta_{\text{ein}}$), without employing inner strong lensing information.

We use the non-parametric deprojection method of [Broadhurst & Barkana \(2008\)](#) to derive for each cluster three-dimensional virial quantities ($r_{\text{vir}}, M_{\text{vir}}$) and values of $M_{\Delta} = M_{3\text{D}}(< r_{\Delta})$ within a sphere of a fixed mean interior overdensity Δ with respect to the critical density $\rho_{\text{crit}}(z_d)$ of the universe at the cluster redshift z_d . We first deproject the two-dimensional mass profiles obtained in § 4.4 and derive non-parametric three-dimensional mass profiles $M_{3\text{D}}(< r)$ simply assuming spherical symmetry, following the method introduced by [Broadhurst & Barkana \(2008\)](#). This method is based on the fact that the surface-mass density $\Sigma(R)$ is related to the three-dimensional mass density $\rho(r)$ by an Abel integral transform; or equivalently, one finds that the three-dimensional mass $M_{3\text{D}}(< r)$ out to spherical radius r is written in terms of $\Sigma(R)$ as

$$M_{3\text{D}}(< r) = M_{2\text{D}}(< R_{\min}) + 2\pi \int_{R_{\min}}^r dR R \Sigma(R) - 4 \int_r^{\infty} dR R f\left(\frac{R}{r}\right) \Sigma(R), \quad (19)$$

where $f(x) = (x^2 - 1)^{-1/2} - \tan^{-1}(x^2 - 1)^{-1/2}$ ([Broadhurst & Barkana 2008](#); [Umetsu et al. 2010](#)),¹⁴ and the first term of the right-hand side can be obtained as $M_{2\text{D}}(< R_{\min}) = \pi R_{\min}^2 \Sigma_{\text{crit}} \bar{\kappa}_{\min}$ with $R_{\min} \equiv D_d \theta_{\min}$. The errors are estimated from Monte Carlo simulations based on the full covariance matrix of the lensing convergence profile (for details, see [Umetsu et al. 2010](#)). In Figure 4 we show the non-parametric cumulative projected (blue-hatched) and spherical (gray-shaded) mass profiles, $M_{2\text{D}}(< \theta)$ and $M_{3\text{D}}(< \theta)$, separately for the five clusters.

Table 7 gives a summary of the spherical mass estimates $M_{3\text{D}}(< r_{\Delta})$ corresponding to $\Delta = \Delta_{\text{vir}}, 200$, and 2500 from our non-parametric deprojection analysis, where $\Delta_{\text{vir}} \simeq 110 - 130$ is the virial overdensity of the spherical collapse model evaluated at the cluster redshift z_d . Overall, we find a good agreement between the virial mass estimates from the parametric and non-parametric deprojection approaches (see § 4.7 for the results of gNFW fits to the combined weak and strong lensing data).

Our virial mass estimate of A1689 is obtained as $M_{\text{vir}} = (1.30 \pm 0.21) \times 10^{15} M_{\odot} h^{-1}$ from the combined distortion and magnification profiles, consistent with the results of [Umetsu & Broadhurst \(2008\)](#), who combined strong lensing, weak lensing distortion and magnification data in a full two-dimensional analysis, and derived $M_{\text{vir}} = 1.5^{+0.6}_{-0.3} \times 10^{15} M_{\odot} h^{-1}$, where this

1σ error includes both statistical and systematic uncertainties (see also [Umetsu et al. 2009](#); [Kawaharada et al. 2010](#); [Molnar et al. 2010](#)).¹⁵ This is also in good agreement with the results from the recent high-resolution lensing observations by [Coe et al. \(2010\)](#), $M_{\text{vir}} = (1.4^{+0.4}_{-0.2}) \times 10^{15} M_{\odot} h^{-1}$. These lensing results are consistent with careful dynamical work by [Lemze et al. \(2009a\)](#), who obtained a virial mass estimate of $M_{\text{vir}} = (1.3 \pm 0.4) \times 10^{15} M_{\odot} h^{-1}$ for A1689. As found early by [Broadhurst et al. \(2008\)](#), our comprehensive weak-lensing analysis implies A370 is the most massive cluster now known, $M_{\text{vir}} = (2.40 \pm 0.25) \times 10^{15} M_{\odot} h^{-1}$. Our virial mass estimate is slightly higher than that derived in our earlier weak-lensing work combined with the inner Einstein radius information, $M_{\text{vir}} = (2.1 \pm 0.2) \times 10^{15} M_{\odot} h^{-1}$ ([Broadhurst et al. 2008](#)), where the difference is primarily due to our improved background selection and depth estimate presented in [Medezinski et al. \(2010\)](#). For RXJ1347-11, we find its NFW virial mass is slightly overestimated compared to the non-parametric estimate of $M_{\text{vir}} = (1.15 \pm 0.25) \times 10^{15} M_{\odot} h^{-1}$ due to the projection of subclumps associated with the large scale structure around the cluster (see [Lu et al. 2010](#)). Our non-parametric mass estimates are in good agreement with independent X-ray, dynamical and lensing analyses ([Kling et al. 2005](#); [Miranda et al. 2008](#); [Lu et al. 2010](#)). For A1703 and Cl0024+17, our new mass estimates are fully consistent with our recent weak-lensing results derived from the Subaru distortion data alone ([Zitrin et al. 2010](#); [Umetsu et al. 2010](#), see also § 4.4).

4.6. Stacking Analysis

The statistical precision of lensing constraints can be further improved by stacking the signal from an ensemble of clusters with respect to their centers, providing average properties of cluster mass profiles. As discussed by [Okabe et al. \(2010\)](#), this stacking analysis has several important advantages. A notable advantage of the stacking analysis is that the resulting average profile is insensitive to the inherent asphericity and substructure (in projection) of individual cluster mass distributions, as well as to uncorrelated large-scale structure projected along the same line of sight. Consequently, the statistical precision can be boosted by stacking together a number of clusters, especially on small angular scales (see [Okabe et al. 2010](#)).

To do this, we first define a new set of radial bands in which the mass profiles of individual clusters are re-evaluated for a stacking analysis. Here we scale each cluster mass profile according to the cluster virial radius r_{vir} obtained by our non-parametric method (see § 4.5). For each cluster, we construct an $M \times N$ projection matrix \mathcal{P}_{ji} that projects the mass profile κ_i ($i = 1, 2, \dots, N$) of the cluster onto the new radial bands scaled in units of r_{vir} ($j = 1, 2, \dots, M$). Assuming a constant density in each radial band, the projection matrix \mathcal{P}_{ji} is uniquely specified by the conservation of mass. With this projection matrix, the mass profile in the new basis is written

¹⁵ Note, without the inner strong lensing information combined, [Umetsu & Broadhurst \(2008\)](#) found $M_{\text{vir}} = (1.38 \pm 0.14) \times 10^{15} M_{\odot} h^{-1}$ (the errors represent only the statistical one) from an entropy-regularized maximum-likelihood combination of Subaru distortion and magnification data sets, in excellent agreement with the one dimensional results in this work.

¹⁴ This integral transformation has an integrable singularity at the lower limit of the second integrand ($R = r$), which can be readily avoided by a suitable coordinate transformation.

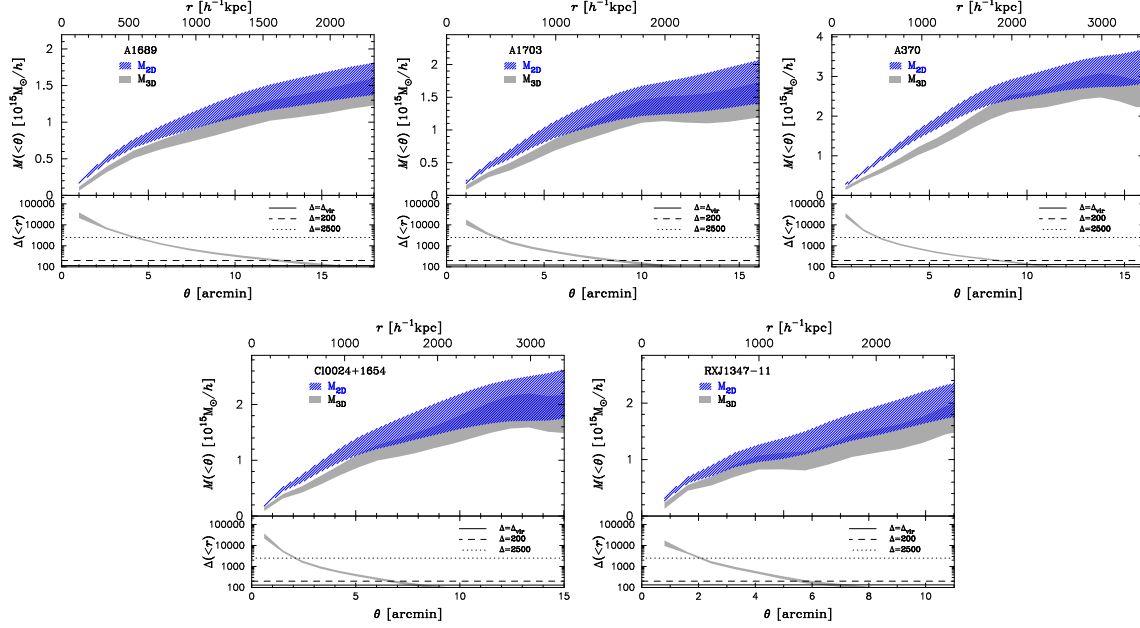


Figure 4. Non-parametric cumulative projected (blue-hatched) and spherical (gray-shaded) mass profiles, $M_{2D}(<\theta)$ and $M_{3D}(<\theta)$, respectively, shown separately for the five clusters. For each cluster, the blue-hatched area in the upper panel shows the 68.3% confidence interval for $M_{2D}(<\theta)$ at each radius estimated from a Monte-Carlo error analysis taking into account the error covariance matrix of the projected mass profile $\kappa(\theta)$ (see Figure 3). Similarly, the gray-shaded area shows the results for the deprojected mass profile $M_{3D}(<\theta)$ assuming spherical symmetry. Shown in the lower panel is the mean spherical overdensity $\bar{\rho}(<r) = M_{3D}(<r)/(4\pi r^3/3)$ interior to radius r in units of the critical density of the universe $\rho_{\text{crit}}(z)$, $\Delta(<r) \equiv \bar{\rho}(<r)/\rho_{\text{crit}}(z)$, reconstructed from our comprehensive weak lensing analysis. The gray-shaded area shows the 68.3% confidence interval at each radius estimated from a Monte-Carlo error analysis taking into account the error covariance matrix of the projected mass profile $\kappa(\theta)$ (see Figure 3). The horizontal solid, dashed, and dotted lines show three representative values for the fractional overdensity, $\Delta = \Delta_{\text{vir}}$, 200, and 2500, respectively, for each cluster. See also Table 7.

Table 7
Three-dimensional Cluster Mass from a Non-parametric Deprojection Analysis.

Cluster	$\Delta = 2500$		$\Delta = 500$		$\Delta = 200$		$\Delta = \Delta_{\text{vir}}$	
	M_{2500} ($10^{15} M_{\odot} h^{-1}$)	r_{2500} ($\text{Mpc } h^{-1}$)	M_{500} ($10^{15} M_{\odot} h^{-1}$)	r_{500} ($\text{Mpc } h^{-1}$)	M_{200} ($10^{15} M_{\odot} h^{-1}$)	r_{200} ($\text{Mpc } h^{-1}$)	M_{vir} ($10^{15} M_{\odot} h^{-1}$)	r_{vir} ($\text{Mpc } h^{-1}$)
A1689	0.569 ± 0.073	0.547 ± 0.025	0.883 ± 0.117	1.083 ± 0.050	1.179 ± 0.170	1.618 ± 0.085	1.300 ± 0.205	2.011 ± 0.113
A1703	0.404 ± 0.069	0.471 ± 0.028	0.787 ± 0.126	1.006 ± 0.058	1.143 ± 0.196	1.546 ± 0.097	1.325 ± 0.221	1.915 ± 0.148
A370	0.529 ± 0.134	0.496 ± 0.040	1.315 ± 0.161	1.152 ± 0.046	2.213 ± 0.270	1.860 ± 0.079	2.399 ± 0.249	2.215 ± 0.079
C10024+17	0.462 ± 0.063	0.472 ± 0.023	0.863 ± 0.136	0.993 ± 0.055	1.194 ± 0.188	1.502 ± 0.081	1.329 ± 0.224	1.799 ± 0.105
RXJ1347-11	0.587 ± 0.060	0.500 ± 0.017	0.949 ± 0.145	1.003 ± 0.051	0.972 ± 0.208	1.373 ± 0.089	1.150 ± 0.250	1.663 ± 0.115

Note. — $M_{\Delta} \equiv M_{3D}(<r_{\Delta})$ is the three-dimensional mass within a sphere of a fixed mean interior overdensity Δ with respect to the critical density of the universe at the cluster redshift z_d .

as

$$\tilde{\kappa} = \mathcal{P}\kappa. \quad (20)$$

Accordingly, the error covariance matrix in the new basis is

$$\tilde{C} = \mathcal{P}C\mathcal{P}^t. \quad (21)$$

With the mass profiles of individual clusters on a common basis, we can stack the clusters to produce an averaged mass profile. Here we re-evaluate the mass profiles of the individual clusters in 8 logarithmically-spaced radial bins over the range of radii $R = [0.05, 1.7]r_{\text{vir}}$. Since the noise in different clusters is uncorrelated, the mass profiles of individual clusters can be co-added according to (e.g., [Sayers et al. 2009](#))

$$\langle \Sigma \rangle = \left(\sum_n \tilde{C}_n^{-1} w_n^2 \right)^{-1} \left(\sum_n \tilde{C}_n^{-1} w_n \tilde{\kappa}_n \right), \quad (22)$$

where the index n runs over all of the clusters, and w_n is the inverse critical surface mass density for the n th cluster, $w_n = (\Sigma_{\text{crit}}^{-1})_n$. The error covariance matrix for the stacked mass profile $\langle \Sigma \rangle$ is obtained as

$$C = \left(\sum_n \tilde{C}_n^{-1} w_n^2 \right)^{-1}, \quad (23)$$

where the index n runs over all of the clusters.

We show in the top panel of Figure 5 the resulting model-independent average mass profile $\langle \Sigma \rangle$ with its statistical 1σ uncertainty as a function of the scaled projected radius R/r_{vir} , obtained by stacking the five clusters using equations (22) and (23) (see also [Mandelbaum et al. 2006](#); [Johnston et al. 2007](#); [Sheldon et al. 2009](#)). We note that the effect of different cluster redshifts has been taken into account by proper

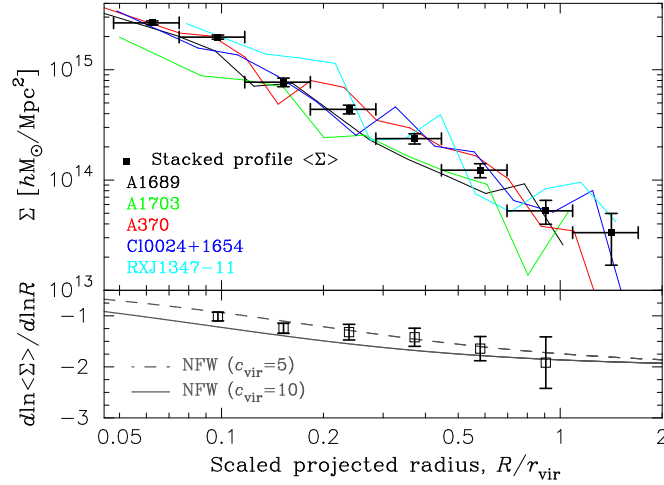


Figure 5. (Top): The model-independent average mass profile $\langle \Sigma \rangle(R)$ (filled squares) with its statistical 1σ uncertainty as a function of the projected radius R scaled with r_{vir} , which is obtained by stacking the lensing convergence profiles for the five clusters, A1689, A1703, A370, Cl0024+17, and RXJ1347-11, shown as solid lines. (Bottom): The logarithmic slope of the stacked mass profile (open squares with error bars), $d \ln \langle \Sigma \rangle / d \ln R$, is shown as a function of the scaled projected radius R/r_{vir} , along with NFW model predictions with $c_{\text{vir}} = 5$ and $c_{\text{vir}} = 10$ for comparison. The projected logarithmic slope steepens from $\gamma_{2D} = -1.01 \pm 0.09$ at $R \approx 0.1 r_{\text{vir}}$ to $\gamma_{2D} = -1.92 \pm 0.51$ at $R \approx 0.9 r_{\text{vir}}$.

error propagation in terms of the lensing efficiency functions (w_n) of individual clusters to average over. The stacked mass profile exhibits a fairly smooth radial trend, and is detected at a high significance level of 37σ out to $R = 1.7 r_{\text{vir}}$.

In the bottom panel of Figure 5, we plot the logarithmic density slope $\gamma_{2D}(R) \equiv d \ln \langle \Sigma \rangle / d \ln R$ of the stacked mass profile as a function of the scaled projected radius along with NFW model predictions with $c_{\text{vir}} = 5$ and $c_{\text{vir}} = 10$. The logarithmic gradient of the average profile shows a slight steepening trend with increasing radius in projection, consistent with NFW profiles with $c_{\text{vir}} = 5 - 10$. Finally, we quote model-independent constraints on the average logarithmic density slope to be $\gamma_{2D} = -1.01 \pm 0.09$ at $R \approx 0.1 r_{\text{vir}}$ and $\gamma_{2D} = -1.92 \pm 0.51$ at $R \approx 0.9 r_{\text{vir}}$ for the five clusters.

4.7. Combining Weak and Strong Lensing

The Subaru data allow the weak lensing profiles of individual clusters to be accurately measured in several independent radial bins in the subcritical regime ($\theta > \theta_{\text{ein}}$). The projected mass profile can be unambiguously recovered on an individual cluster basis from combined weak-lensing shape distortion and magnification bias measurements.

Here we combine our weak-lensing profiles with detailed strong-lensing information for the inner $\lesssim 200$ kpc region of these clusters, for which we have identified many new sets of multiple images from deep *HST*/ACS observations (Broadhurst et al. 2005b; Zitrin et al. 2009, 2010), for a full determination of the entire mass profiles of the five well-studied clusters. Figure 6 shows a sample of joint mass profiles for our five clusters recovered over two decades of radius ranging from $10 \text{ kpc } h^{-1}$ to $3000 \text{ kpc } h^{-1}$. Note in this comparison we have excluded the central weak-lensing bin $\bar{\kappa}(< \theta_{\text{min}})$ and the strong-lensing data points at radii overlapping with the Subaru data. In each case, the weak and strong lensing are in excellent agreement where the data overlap (typically around $R \sim 150 \text{ kpc } h^{-1}$), and the joint mass pro-

files form well-defined radial profiles with a continuously-steepening radial trend from the central region to beyond the virial radius ($\lesssim 1.7 r_{\text{vir}}$).

Our high-quality lensing data, covering the entire cluster, allow us to place useful constraints on the gNFW structure parameters (§ 4.3), namely, the central cusp slope α as well as the NFW virial mass and concentration parameters. Using our full lensing constraints, we obtain for each cluster the best-fit gNFW model as summarized in Table 6. For the halo mass and concentration parameters (M_{vir}, c_{-2}), we find good agreement between the results with and without the inner strong-lensing profile combined (for Cl0024+17, see also Umetsu et al. 2010). Our joint mass profiles for the entire cluster region are consistent with a generalized form of the NFW density profile with modest variations in the central cusp slope ($\alpha \lesssim 0.9$), except for the ongoing merger RXJ1347-11 (see Mason et al. 2010), for which we find an unacceptable fit with a reduced χ^2 of 58 for 28 degrees of freedom, due to various local deviations from the model, especially in the inner mass profile which is tightly constrained by strong lensing. The best-fit value of α derived for the relaxed cluster A1703 is $\alpha = 0.93^{+0.19}_{-0.25}$, being consistent with NFW ($\alpha = 1$), which is in excellent agreement with independent lensing results by Oguri et al. (2009), $\alpha = 0.9^{+0.2}_{-0.4}$, and Richard et al. (2009), $\alpha = 0.92^{+0.05}_{-0.04}$.

5. SUMMARY AND DISCUSSION

We have developed a new method for a direct reconstruction of the projected mass profile of galaxy clusters from combined weak-lensing distortion and magnification measurements (§ 3.1 and § 3.2) within a Bayesian statistical framework, which allows for a full parameter-space extraction of the underlying signal. This method applies to the full range of radius outside the Einstein radius, where nonlinearity between the surface mass density and the observables extends to a radius of a few arcminutes, and recovers the absolute mass normalization. A proper Bayesian statistical analysis is essential to explore the entire parameter space and investigate the parameter de-

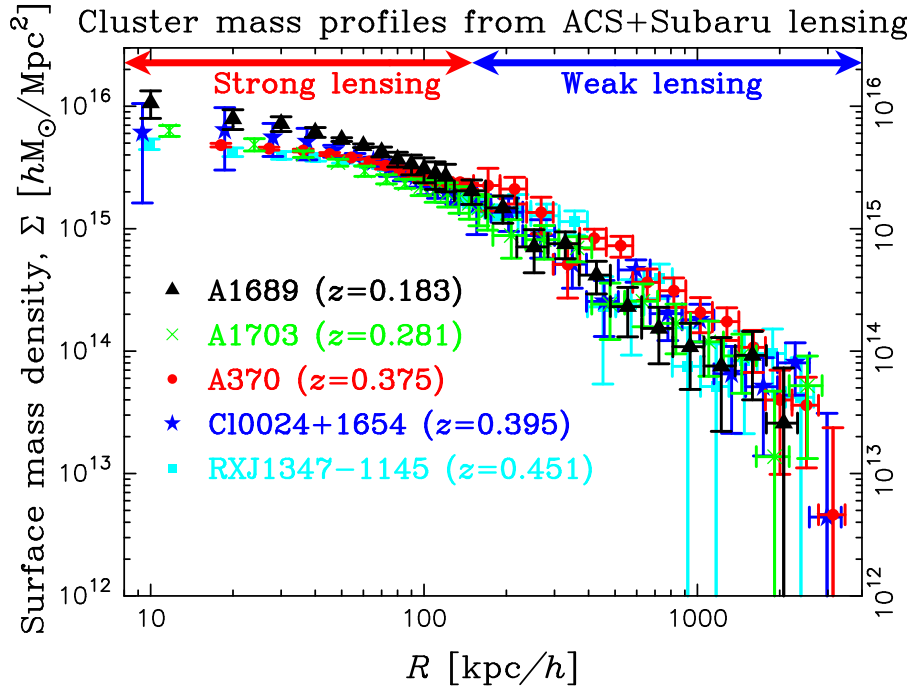


Figure 6. Full mass profiles for A1689 (triangles), A1703 (crosses), A370 (circles), Cl0024+17 (stars), and RXJ1347-11 (squares) over a wide range of radius, from $10 \text{ kpc } h^{-1}$ to $3000 \text{ kpc } h^{-1}$, derived from ACS strong-lensing ($R \lesssim 150 \text{ kpc } h^{-1}$) and Subaru weak-lensing ($R \gtrsim 150 \text{ kpc } h^{-1}$) measurements, showing a continuously steepening radial trend out to and beyond the cluster virial radius ($r_{\text{vir}} \sim 2 \text{ Mpc } h^{-1}$).

generacies (§ 3.3), arising from the mass-sheet degeneracy (§ 2). This method can be readily generalized for a statistical analysis using stacked lensing profiles of a sample of clusters.

We have applied our comprehensive lensing method to a sample of five high-mass clusters for which detailed strong-lensing information is readily available from *HST*/ACS observations. The deep Subaru multi-band photometry, in conjunction with our background-selection techniques (Medezinski et al. 2010; Umetsu et al. 2010), allows for a secure selection of uncontaminated blue and red background populations. In each cluster, a strong depletion of the red galaxy counts has been detected at a significance level of 6σ – 11σ (Table 5). A comparison shows clear consistency between two independent lensing observables with different systematics, ensuring the reliability of our weak-lensing analysis (Figure 1). The combination of independent Subaru distortion and magnification data breaks the mass-sheet degeneracy, as examined by our Bayesian statistical analysis (Figure 2). Excluding magnification data, on the other hand, strongly modifies the Gaussian shape of the marginalized posterior PDFs, producing long non-Gaussian tails and broadening the distribution function, resulting in large reconstruction errors. The improvement here from adding the magnification measurements is significant, $\sim 30\%$ in terms of cluster mass profile measurements (Table 5).

We have formed a model-independent mass profile from stacking the clusters, which is detected at 37σ out to beyond the virial radius, $R \approx 1.7r_{\text{vir}}$. We found that the projected logarithmic slope, $\gamma_{2D}(R) = d \ln \Sigma(R) / d \ln R$, steepens from $\gamma_{2D} = -1.01 \pm 0.09$ at $R \approx 0.1r_{\text{vir}}$ to $\gamma_{2D} = -1.92 \pm 0.51$ at $R \approx 0.9r_{\text{vir}}$, consistent with

NFW profiles with $c_{\text{vir}} = 5 - 10$. We also obtained for each cluster inner strong-lensing based mass profiles from deep *HST*/ACS observations, which we have shown overlap well with the outer Subaru-based profiles and together are well described by a generalized Navarro-Frenk-White profile, except for the ongoing merger RXJ1347-11 (Mason et al. 2010), with modest variations in the central cusp slope ($\alpha \lesssim 0.9$), perhaps related to the dynamical state of the cluster.

These high-mass lensing clusters with large Einstein radii appear to be centrally concentrated in projection, as found in several other well studied massive clusters from careful lensing work (Gavazzi et al. 2003; Kneib et al. 2003; Broadhurst et al. 2005a; Limousin et al. 2007; Broadhurst et al. 2008; Broadhurst & Barkana 2008; Oguri et al. 2009; Umetsu et al. 2010; Zitrin et al. 2011). An accurate characterization of the observed sample is crucial for any cluster-based cosmological tests. It has been suggested that clusters selected with giant arcs represent a highly biased population in the context of Λ CDM. For those clusters with large Einstein radii (say, $\theta_{\text{ein}} > 20''$), a large statistical bias of about $(40 - 60)\%$ is derived from *N*-body simulations (Hennawi et al. 2007; Oguri & Blandford 2009), representing the most triaxial cases. The mean level of mass concentration inferred from our weak lensing analysis is high, $\langle c_{\text{vir}} \rangle = 7.9 \pm 0.8$ (simply ignoring the mass and redshift dependencies), for our sample with $\langle M_{\text{vir}} \rangle = (1.48 \pm 0.10) \times 10^{15} M_{\odot} h^{-1}$, as compared to the Λ CDM predictions, $\langle c_{\text{vir}} \rangle = 3.4^{+1.5}_{-1.0}$ (the errors quoted represent a 1σ lognormal scatter of $\sigma(\log_{10} c_{\text{vir}}) = 0.15$; see Duffy et al. 2008), evaluated at the median redshift of our sample, $\bar{z}_d \approx 0.38$. This represents an overall discrepancy of 5σ with respect to the

predictions, without taking into account the effects of projection bias. This apparent discrepancy is also evident when the weak-lensing mass profiles are combined with the inner strong-lensing information from deep ACS observations (§ 4.7). Applying a bias correction of 50% (see Broadhurst et al. 2008; Oguri et al. 2009), the discrepancy in $\langle c_{\text{vir}} \rangle$ is reduced to the 3σ level.

Another possible source of systematic errors in the mass profile determination is the cluster off-centering effect (§ 4.3). The effect is essentially the smoothing of the central lensing signal (see Oguri & Takada 2011), which flattens the recovered convergence profile below the offset scale, and therefore reduces the derived mass concentration (c_{-2}) and cusp slope (α) parameters. For our sample of clusters, we found a cluster centering offset of typically $\Delta\theta \lesssim 5''$ using our detailed strong-lensing models. This level of centering offset ($\Delta R \lesssim 20 \text{ kpc } h^{-1}$) is much smaller than the estimated values for the inner characteristic radius of our clusters, $r_{-2} \sim 200 \text{ kpc } h^{-1}$, and hence may not significantly affect our concentration measurements. However, this could potentially lead to an underestimation of the central cusp slope α .

Our results are consistent with previous lensing work which similarly detected a concentration excess in the lensing-based measurements for strong-lensing clusters (Comerford & Natarajan 2007; Broadhurst et al. 2008;

Oguri et al. 2009). Our findings could imply, for these clusters, either substantial mass projected along the line of sight, due in part to intrinsic halo triaxiality, or a higher-than-expected concentration of dark matter. Nevertheless, the overall level of uncertainties may be too large to robustly test the CDM predictions with the present sample. The forthcoming space telescope cluster survey, CLASH¹⁶, will provide a definitive derivation of mass profiles for a larger, lensing-unbiased sample of relaxed X-ray clusters ($> 5 \text{ keV}$), combining high-resolution panchromatic space imaging with deep, wide-field Subaru weak-lensing observations, for a definitive determination of the representative mass profile of massive clusters.

We thank the anonymous referee for a careful reading of the manuscript and for providing invaluable comments. We are very grateful for discussions with Doron Lemze, Sandor Molnar, Masahiro Takada, Masayuki Tanaka, Nobuhiro Okabe, and Sherry Suyu, whose comments were very helpful. K.U. acknowledges Yuji Chinone for helpful comments on MCMC techniques. We thank Nick Kaiser for making the IMCAT package publicly available. The work is partially supported by the National Science Council of Taiwan under the grant NSC97-2112-M-001-020-MY3.

APPENDIX

A. MASKING CORRECTION

For the cluster magnification analysis, the masking effect due to bright cluster galaxies, bright foreground objects, and saturated objects has to be properly taken into account and corrected for (Broadhurst et al. 2005a; Umetsu & Broadhurst 2008; Umetsu et al. 2010). Here we describe two different approaches for estimating the effect of masking in the magnification bias measurement.

A.1. Method A

In this method (Method A), we describe each masking object as an ellipse specified by its structure parameters, such as the size, axis ratio, and position angle. SExtractor provides such useful estimates of object properties (magnitude, size, axis ratio, position angle, and so on) for calculating masking areas and the resulting correction. In practice, we account for the masking of observed sky by excluding a generous area πab around each masking object, where a and b are defined as $\nu_{\text{mask}} (= 2 - 4)$ times the major (A_IMAGE) and minor axes (B_IMAGE) computed from SExtractor, corresponding roughly to the isophotal detection limit (see Umetsu & Broadhurst (2008) and Umetsu et al. (2010)). We then calculate the correction factor for this masking effect as a function of radius from the cluster center, and renormalize the number density accordingly. Note that the actual choice of ν_{mask} is insensitive to the resulting magnification measurement $n_{\mu}/n_0 = \mu^{2.5s-1}$ (Umetsu & Broadhurst 2008; Umetsu et al. 2010), as this effect will cancel out when taking a ratio of the local surface density n_{μ} to the unlensed mean number density n_0 (see § 5.5.3 of Umetsu & Broadhurst 2008). However, this method is not suitable for estimating masking areas by saturated stars and stellar trails, which cannot be described by simple ellipses. For this case, we manually place a rectangular region mask around each saturated object to exclude a proper area. This approach has been commonly adopted in previous studies of cluster magnification bias (Taylor et al. 1998; Broadhurst et al. 2005a; Umetsu & Broadhurst 2008; Umetsu et al. 2010).

In the top panel of Figure 7, we show as an example the masked region in A1689 based on the Subaru i' -band photometry, as obtained using Method A (see also Umetsu & Broadhurst 2008). The gray area shows bright masking objects ($i' < 22 \text{ AB mag}$), each described as an ellipse. The black rectangular regions are masked areas for saturated stars and bright stellar trails. We show in Figure 8 the level of mask area correction in A1689 as a function of radius from the cluster center. The masking area is negligible (a few %) at large radii, and increases up to $\sim 20\%$ of the sky close to the cluster center. Typically, the level of masking correction is found to be sufficiently small ($\ll 1$), so that the uncertainty in the masking correction is of the second order, and hence negligible.

A.2. Method B

Here we describe an alternative method (Method B) for the masking correction which we have developed in this work. This method has practical advantages in comparison to Method A: that is, it is easy to implement and can be

¹⁶ Cluster Lensing And Supernova Survey with Hubble (P.I.: M. Postman), <http://www.stsci.edu/~postman/CLASH/>

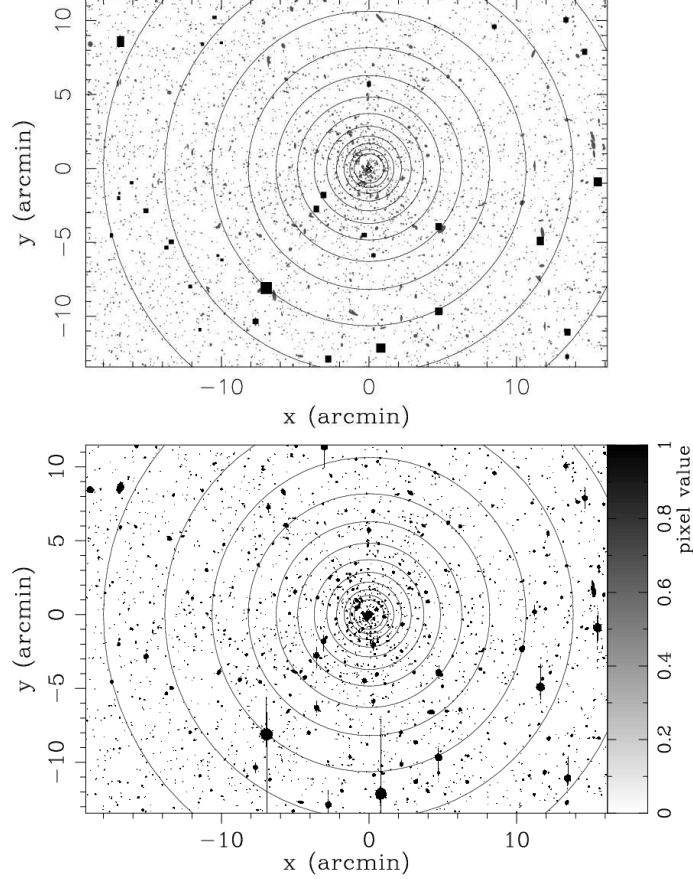


Figure 7. Distribution of masked regions in A1689 ($z = 0.183$). Superposed are the concentric radial bands used for calculating the radial profiles centered on the BCG. *Top:* Results obtained using Method A (see Appendix A.1). The gray area shows bright masking objects ($i' < 22$ AB mag), each described as an ellipse. The black rectangular regions are masked areas for saturated stars and bright stellar trails. *Bottom:* Results obtained using Method B (see Appendix A.2) based on SExtractor’s check-image output with `CHECKIMAGE_TYPE = OBJECT`. The black area shows those connected pixels that belong to bright foreground objects, bright cluster galaxies, saturated stars, and stellar trails.

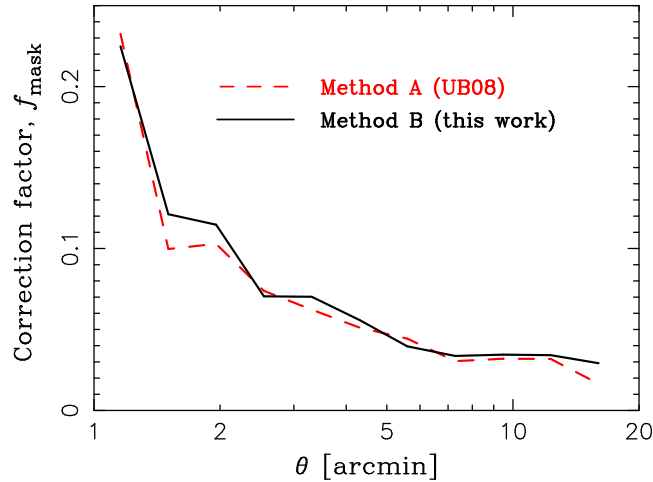


Figure 8. The azimuthally-averaged correction factor $f_{\text{mask}}(\theta)$ for the masking effect as a function of radius from the center of A1689. The red dashed curve shows the level of correction required due to masking, as estimated by Umetsu & Broadhurst (2008) using Method A (Appendix A.1). The black solid curve shows the results using Method B (Appendix A.2). The two methods give consistent results in terms of both shape and amplitude of the radial profile of the correction factor.

fully automated once the configuration of analysis parameters is tuned, especially useful for large scale sky surveys such as the Subaru HSC survey.

In this approach, we use a pixelized flag image to exclude masking regions, namely those connected pixels that

belong to bright foreground objects, bright cluster galaxies, saturated stars, and stellar trails. This can be done using SExtractor's check-image output with `CHECKIMAGE_TYPE = OBJECTS`. We tune SExtractor configuration's detection parameters in order to optimize the detection for a particular object size and brightness. In our analysis of Subaru images, the per-pixel detection threshold above the local sky background is set to 5σ (`DETECT_THRESH = 5`), and the minimum number of connected pixels above threshold is set to 300 (`DETECT_MINAREA = 300`) with $0.202''$ pixel $^{-1}$ sampling. The bottom panel of Figure 7 shows the distribution of masked regions in A1689 as obtained using Method B. Figure 8 compares the masking correction factor in A1689 obtained using Methods A and B, shown as a function of radius from the cluster center. It is shown that the two methods give consistent results in terms of both shape and amplitude of the radial profile of the correction factor.

B. DISCRETIZED ESTIMATOR FOR THE AVERAGED CONVERGENCE

In this Appendix, we aim to derive a discrete expression for the mean interior convergence $\bar{\kappa}(< \theta)$ using the azimuthally-averaged convergence $\kappa(\theta)$. In the continuous limit, the mean convergence $\bar{\kappa}(< \theta)$ interior to radius θ can be expressed in terms of $\kappa(\theta)$ as

$$\bar{\kappa}(\theta) = \frac{2}{\theta^2} \int_0^\theta d \ln \theta' \theta'^2 \kappa(\theta'). \quad (\text{B1})$$

For a given set of $(N + 1)$ annular radii θ_l ($l = 1, 2, \dots, N + 1$), defining N radial bands in the range $\theta_{\min} \equiv \theta_1 \leq \theta \leq \theta_{N+1} \equiv \theta_{\max}$, a discretized estimator for $\bar{\kappa}(< \theta)$ can be written in the following way:

$$\bar{\kappa}(< \theta_l) = \frac{\theta_{\min}^2}{\theta_l^2} \bar{\kappa}(< \theta_{\min}) + \frac{2}{\theta_l^2} \sum_{i=1}^{l-1} \Delta \ln \theta_i \bar{\theta}_i^2 \kappa(\bar{\theta}_i), \quad (\text{B2})$$

with $\Delta \ln \theta_i \equiv (\theta_{i+1} - \theta_i)/\bar{\theta}_i$ and $\bar{\theta}_i$ being the area-weighted center of the i th annulus defined by θ_i and θ_{i+1} ; in the continuous limit, we have

$$\begin{aligned} \bar{\theta}_i &\equiv 2 \int_{\theta_i}^{\theta_{i+1}} d\theta' \theta'^2 / (\theta_{i+1}^2 - \theta_i^2) \\ &= \frac{2}{3} \frac{\theta_i^2 + \theta_{i+1}^2 + \theta_i \theta_{i+1}}{\theta_i + \theta_{i+1}}. \end{aligned} \quad (\text{B3})$$

C. DISCRETIZED ESTIMATORS FOR THE LENSING PROFILES

We derive expressions for the binned tangential distortion g_+ and magnification μ in terms of the binned convergence κ , using the following relations:

$$g_+(\bar{\theta}_i) = \frac{\bar{\kappa}(< \bar{\theta}_i) - \kappa(\bar{\theta}_i)}{1 - \kappa(\bar{\theta}_i)}, \quad (\text{C1})$$

$$\mu(\bar{\theta}_i) = \frac{1}{(1 - \kappa(\bar{\theta}_i))^2 (1 - g_+^2(\bar{\theta}_i))}, \quad (\text{C2})$$

where both the quantities depend on the mean convergence $\bar{\kappa}$ interior to the radius $\bar{\theta}_i$, which is the center of the i th radial band of $[\theta_i, \theta_{i+1}]$ (see Appendix B). By assuming a constant density in each radial band and by noting that $\bar{\theta}_i$ is the *median* radius of the i th radial band, $\bar{\kappa}(< \bar{\theta}_i)$ can be well approximated by

$$\bar{\kappa}(< \bar{\theta}_i) = \frac{1}{2} \left(\bar{\kappa}(< \theta_i) + \bar{\kappa}(< \theta_{i+1}) \right) \quad (\text{C3})$$

where $\bar{\kappa}(< \theta_i)$ and $\bar{\kappa}(< \theta_{i+1})$ can be computed using the formulae given in Appendices B and C.

If we are to combine background samples of different populations (a and b) and different lensing depths $\langle \beta \rangle$, we should take into account population-to-population variations in the lensing depth, $\omega_{ba} = \langle \beta \rangle_b / \langle \beta \rangle_a$, which can be measured from deep multi-band imaging, such as the 30-band COSMOS database (Ilbert et al. 2009). The tangential distortion $g_+^{(b)}$ for Population (b) can be expressed in terms of the convergence $\kappa^{(a)}$ for Population (a) as

$$g_+^{(b)} = \frac{\omega_{ba} (\bar{\kappa}^{(a)} - \kappa^{(a)})}{(1 - \omega_{ba} \kappa^{(a)})}. \quad (\text{C4})$$

Similarly, the magnification $\mu^{(b)}$ for Population (b) can be expressed in terms of $\omega_{ba} \kappa^{(a)}$.

D. SUPPLEMENTAL MATERIAL

In this supplemental material section, we compare observed tangential-distortion (shear) g_+ and count-depletion (magnification) n_μ radial profiles with their respective reconstructed profiles, taking A370 at $z_d = 0.375$ (Figure 9) and Cl0024+17 at $z_d = 0.395$ (Figure 10) as examples. We note that this supplemental material is added for the arXiv version only, and is not included in the published ApJ version (Umetsu et al. 2011, ApJ, 729, 127).

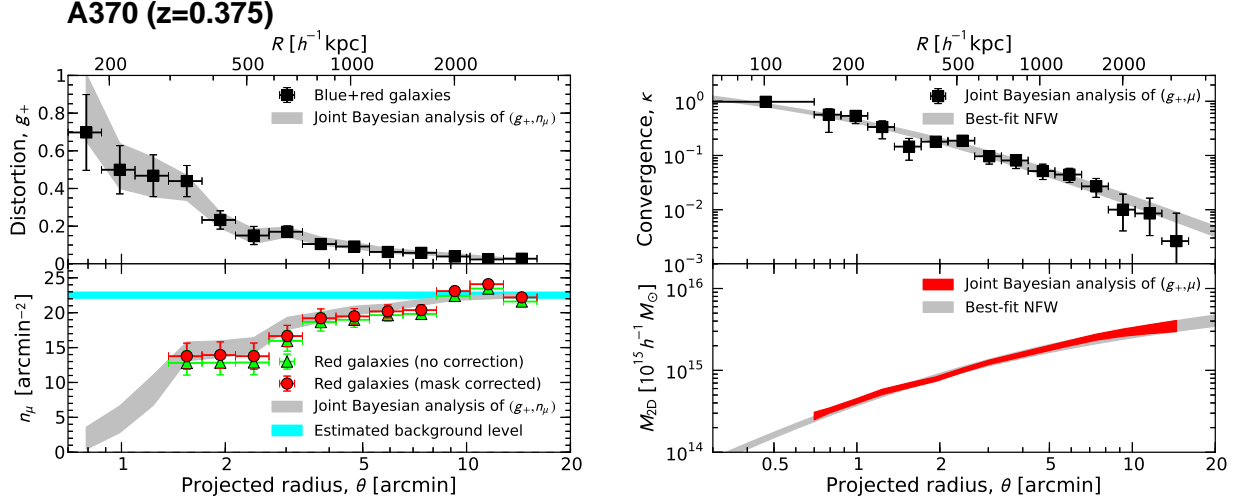


Figure 9. **Left:** weak-lensing radial profiles of A370 ($z_d = 0.375$) as measured from background galaxies registered in Subaru $B_j R_c z'$ images (Table 1). The top panel shows the tangential reduced shear profile $g_+(\theta)$ (squares) based on Subaru distortion data of the full background (red+blue) sample (Table 3). The bottom panel shows the count depletion profiles $n_\mu(\theta)$ due to magnification for a flux-limited sample of red background galaxies. The circles and triangles show the respective results with and without the mask correction due to bright foreground objects and cluster members. The horizontal bar represents the constraints on the unlensed count normalization, n_0 , as estimated from Subaru data. Also shown in each panel is the joint Bayesian fit (gray area, 68% CL) to both profiles, **Right:** the *joint mass profile solution* of the shear and magnification data sets shown in the left panels, obtained following the Bayesian method described in the main text (Section 3), effectively breaking the mass-sheet degeneracy. The top panel shows the reconstructed surface mass density profile $\kappa = \Sigma/\Sigma_{\text{crit}}$ (squares), in good agreement with the standard NFW form (gray area, 68% CL; see Table 6). The innermost bin represents the average surface mass density $\bar{\kappa}_{\text{min}} \equiv \bar{\kappa}(<\theta_{\text{min}})$ interior to the inner radial boundary $\theta_{\text{min}} = 0.7'$ of the weak-lensing distortion data. The bottom panel shows the projected cumulative mass profile M_{2D} (red), along with the best-fit NFW model (gray area, 68% CL; Table 6).

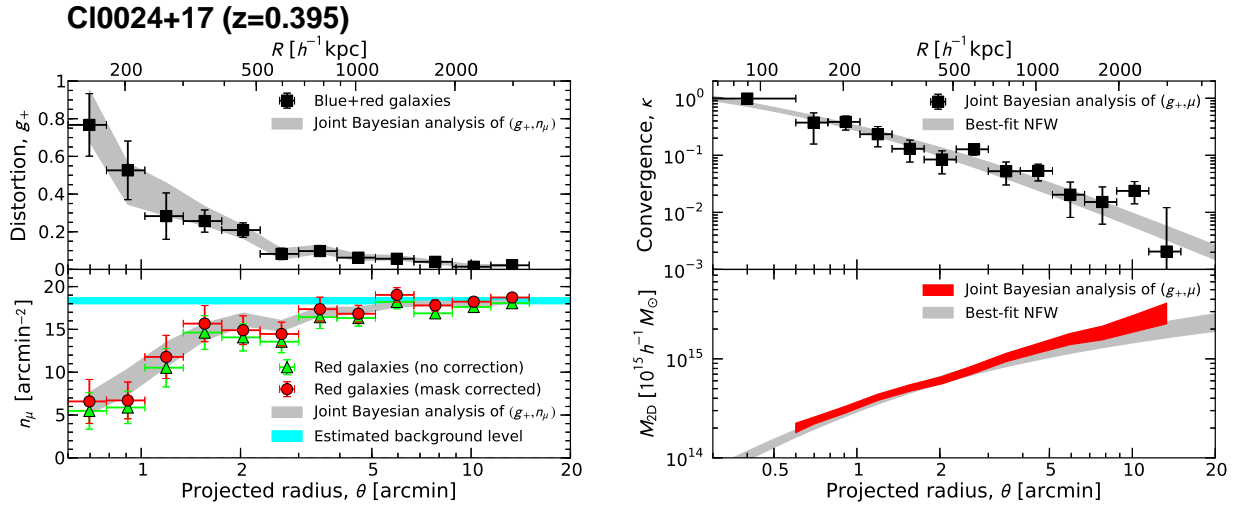


Figure 10. Same as in Figure 9, but shown for the cluster Cl0024+17 ($z_d = 0.395$). A strong depletion of the red galaxy counts is clearly detected (bottom left panel) down to the inner radial boundary of the weak lensing data, $\theta_{\text{min}} = 0.6'$. A consistent mass profile solution $\mathbf{s} = \{\bar{\kappa}_{\text{min}}, \kappa_i\}_{i=1}^N$ (top right panel) is obtained from a joint Bayesian fit to both lensing profiles shown in the left panels.

REFERENCES

- Bartelmann, M., & Schneider, P. 1999, *A&A*, 345, 17
- . 2001, *Phys. Rep.*, 340, 291
- Bradač, M., Schrabback, T., Erben, T., et al. 2008, *ApJ*, 681, 187
- Broadhurst, T., Takada, M., Umetsu, K., et al. 2005a, *ApJ*, 619, L143
- Broadhurst, T., Umetsu, K., Medezinski, E., Oguri, M., & Rephaeli, Y. 2008, *ApJ*, 685, L9
- Broadhurst, T., Benítez, N., Coe, D., et al. 2005b, *ApJ*, 621, 53
- Broadhurst, T. J., & Barkana, R. 2008, *MNRAS*, 390, 1647
- Broadhurst, T. J., Taylor, A. N., & Peacock, J. A. 1995, *ApJ*, 438, 49
- Clowe, D., Bradač, M., Gonzalez, A. H., et al. 2006, *ApJ*, 648, L109
- Coe, D., Benítez, N., Broadhurst, T., & Moustakas, L. A. 2010, *ApJ*, 723, 1678
- Comerford, J. M., & Natarajan, P. 2007, *MNRAS*, 379, 190
- Duffy, A. R., Schaye, J., Kay, S. T., & Dalla Vecchia, C. 2008, *MNRAS*, 390, L64
- Dunkley, J., Bucher, M., Ferreira, P. G., Moodley, K., & Skordis, C. 2005, *MNRAS*, 356, 925
- Evrard, A. E., MacFarland, T. J., Couchman, H. M. P., et al. 2002, *ApJ*, 573, 7
- Fukushige, T., & Makino, J. 1997, *ApJ*, 477, L9+
- Gavazzi, R., Fort, B., Mellier, Y., Pelló, R., & Dantel-Fort, M. 2003, *A&A*, 403, 11
- Gelman, A., & Rubin, D. B. 1992, *Statist. Sci.*, 7, 457
- Ghigna, S., Moore, B., Governato, F., et al. 1998, *MNRAS*, 300, 146
- Goldberg, D. M., & Bacon, D. J. 2005, *ApJ*, 619, 741
- Halkola, A., Hildebrandt, H., Schrabback, T., et al. 2008, *A&A*, 481, 65
- Hamana, T., Miyazaki, S., Shimasaku, K., et al. 2003, *ApJ*, 597, 98
- Hattori, M., Kneib, J., & Makino, N. 1999, *Progress of Theoretical Physics Supplement*, 133, 1
- Hennawi, J. F., Dalal, N., Bode, P., & Ostriker, J. P. 2007, *ApJ*, 654, 714
- Hoekstra, H., Franx, M., & Kuijken, K. 2000, *ApJ*, 532, 88
- Ilbert, O., Capak, P., Salvato, M., et al. 2009, *ApJ*, 690, 1236
- Jain, B., Seljak, U., & White, S. 2000, *ApJ*, 530, 547
- Jee, M. J., White, R. L., Benítez, N., et al. 2005, *ApJ*, 618, 46
- Jee, M. J., Rosati, P., Ford, H. C., et al. 2009, *ApJ*, 704, 672
- Jing, Y. P., & Suto, Y. 2000, *ApJ*, 529, L69
- Johnston, D. E., Sheldon, E. S., Wechsler, R. H., et al. 2007, *arXiv*, 0709.1159
- Kaiser, N., Squires, G., & Broadhurst, T. 1995, *ApJ*, 449, 460
- Kawaharada, M., Okabe, N., Umetsu, K., et al. 2010, *ApJ*, 714, 423
- Keeton, C. R. 2001, *ArXiv Astrophysics e-prints*, arXiv:astro-ph/0102341
- Kling, T. P., Dell’Antonio, I., Wittman, D., & Tyson, J. A. 2005, *ApJ*, 625, 643
- Kneib, J.-P., Hudelot, P., Ellis, R. S., et al. 2003, *ApJ*, 598, 804
- Lemze, D., Barkana, R., Broadhurst, T. J., & Rephaeli, Y. 2008, *MNRAS*, 386, 1092
- Lemze, D., Broadhurst, T., Rephaeli, Y., Barkana, R., & Umetsu, K. 2009a, *ApJ*, 701, 1336
- Lemze, D., Rephaeli, Y., Barkana, R., et al. 2011, *ApJ*, 728, 40
- Lemze, D., Sadeh, S., & Rephaeli, Y. 2009b, *MNRAS*, 397, 1876
- Limousin, M., Richard, J., Jullo, E., et al. 2007, *ApJ*, 668, 643
- Limousin, M., Richard, J., Kneib, J., et al. 2008, *A&A*, 489, 23
- Lu, T., Gilbank, D. G., Balogh, M. L., et al. 2010, *MNRAS*, 403, 1787
- Mandelbaum, R., Seljak, U., Cool, R. J., et al. 2006, *MNRAS*, 372, 758
- Markevitch, M., Gonzalez, A. H., Clowe, D., et al. 2004, *ApJ*, 606, 819
- Markevitch, M., Gonzalez, A. H., David, L., et al. 2002, *ApJ*, 567, L27
- Marshall, P. J., Hobson, M. P., Gull, S. F., & Bridle, S. L. 2002, *MNRAS*, 335, 1037
- Mason, B. S., Dicker, S. R., Korngut, P. M., et al. 2010, *ApJ*, 716, 739
- Massey, R., Heymans, C., Bergé, J., et al. 2007, *MNRAS*, 376, 13
- Mastropietro, C., & Burkert, A. 2008, *MNRAS*, 389, 967
- Mead, J. M. G., King, L. J., Sijacki, D., et al. 2010, *MNRAS*, 406, 434
- Medezinski, E., Broadhurst, T., Umetsu, K., et al. 2010, *MNRAS*, 405, 257
- . 2007, *ApJ*, 663, 717
- Meneghetti, M., Fedeli, C., Pace, F., Gottlöber, S., & Yepes, G. 2010a, *A&A*, 519, A90+
- Meneghetti, M., Rasia, E., Merten, J., et al. 2010b, *A&A*, 514, A93+
- Merten, J., Cacciato, M., Meneghetti, M., Mignone, C., & Bartelmann, M. 2009, *A&A*, 500, 681
- Miranda, M., Sereno, M., de Filippis, E., & Paolillo, M. 2008, *MNRAS*, 385, 511
- Miyazaki, S., Komiyama, Y., Sekiguchi, M., et al. 2002, *PASJ*, 54, 833
- Molnar, S. M., Chiu, I.-N., Umetsu, K., et al. 2010, *ApJ*, 724, L1
- Navarro, J. F., Frenk, C. S., & White, S. D. M. 1996, *ApJ*, 462, 563
- . 1997, *ApJ*, 490, 493
- Navarro, J. F., Hayashi, E., Power, C., et al. 2004, *MNRAS*, 349, 1039
- Neto, A. F., Gao, L., Bett, P., et al. 2007, *MNRAS*, 381, 1450
- Oguri, M., & Blandford, R. D. 2009, *MNRAS*, 392, 930
- Oguri, M., & Takada, M. 2011, *Phys. Rev. D*, 83, 023008
- Oguri, M., Takada, M., Okabe, N., & Smith, G. P. 2010, *MNRAS*, 405, 2215
- Oguri, M., Takada, M., Umetsu, K., & Broadhurst, T. 2005, *ApJ*, 632, 841
- Oguri, M., Hennawi, J. F., Gladders, M. D., et al. 2009, *ApJ*, 699, 1038
- Okabe, N., Takada, M., Umetsu, K., Futamase, T., & Smith, G. P. 2010, *PASJ*, 62, 811
- Okabe, N., & Umetsu, K. 2008, *PASJ*, 60, 345
- Okamoto, T., & Habe, A. 1999, *ApJ*, 516, 591
- Okura, Y., Umetsu, K., & Futamase, T. 2007, *ApJ*, 660, 995
- . 2008, *ApJ*, 680, 1
- Power, C., Navarro, J. F., Jenkins, A., et al. 2003, *MNRAS*, 338, 14
- Richard, J., Kneib, J., Limousin, M., Edge, A., & Jullo, E. 2010, *MNRAS*, 402, L44
- Richard, J., Pei, L., Limousin, M., Jullo, E., & Kneib, J. P. 2009, *A&A*, 498, 37
- Rines, K., & Geller, M. J. 2008, *AJ*, 135, 1837
- Rozo, E., & Schmidt, F. 2010, *arXiv*, 1009.5735
- Sadeh, S., & Rephaeli, Y. 2008, *MNRAS*, 388, 1759
- Sayers, J., Golwala, S. R., Rossinot, P., et al. 2009, *ApJ*, 690, 1597
- Schneider, P., & Seitz, C. 1995, *A&A*, 294, 411
- Sheldon, E. S., Johnston, D. E., Scranton, R., et al. 2009, *ApJ*, 703, 2217
- Sheth, R. K., Mo, H. J., & Tormen, G. 2001, *MNRAS*, 323, 1
- Tasitsiomi, A., Kravtsov, A. V., Gottlöber, S., & Klypin, A. A. 2004, *ApJ*, 607, 125
- Taylor, A. N., Dye, S., Broadhurst, T. J., Benitez, N., & van Kampen, E. 1998, *ApJ*, 501, 539
- Umetsu, K. 2010, *arXiv*, 1002.3952
- Umetsu, K., & Broadhurst, T. 2008, *ApJ*, 684, 177
- Umetsu, K., & Futamase, T. 2000, *ApJ*, 539, L5
- Umetsu, K., Medezinski, E., Broadhurst, T., et al. 2010, *ApJ*, 714, 1470
- Umetsu, K., Tada, M., & Futamase, T. 1999, *Progress of Theoretical Physics Supplement*, 133, 53
- Umetsu, K., Birkinshaw, M., Liu, G.-C., et al. 2009, *ApJ*, 694, 1643
- Van Waerbeke, L., Hildebrandt, H., Ford, J., & Milkeraitis, M. 2010, *ApJ*, 723, L13
- Zhang, P., & Pen, U. 2005, *Physical Review Letters*, 95, 241302
- Zhao, H. 1996, *MNRAS*, 278, 488
- Zitrin, A., Broadhurst, T., Barkana, R., Rephaeli, Y., & Benítez, N. 2011, *MNRAS*, 410, 1939
- Zitrin, A., Broadhurst, T., Umetsu, K., et al. 2009, *MNRAS*, 396, 1985
- . 2010, *MNRAS*, 408, 1916